Prior heterogeneous ice nucleation events increase likelihood of shape homogeneous freezing during the evolution of synoptic cirrus

Kasper Juurikkala^{1,2}, Christina J. Williamson^{1,3}, Karl D. Froyd^{4,5}, Jonathan Dean-Day⁶, and Ari Laaksonen^{1,7}

Correspondence: Kasper Juurikkala (kasper.juurikkala@fmi.fi)

Abstract. In-situ In situ observations are currently used to classify synoptic cirrus as formed by homogeneous or heterogeneous ice nucleation based on ice residual analysis. We use large-eddy model UCLALES-SALSA to show the limitations of this method by demonstrating that prior heterogeneous ice nucleation freezing events can shape the thermodynamic conditions for homogeneous freezing to occur more likely in the subsequent nucleation events.

In a single-cloud case study of synoptic cirrus from NASA's Midlatitude Airborne Cirrus Properties Experiment (MACPEX), observations suggest homogeneous freezing as the dominant nucleation mechanism. Simulations done with UCLALES-SALSA show that homogeneous freezing occurred after earlier heterogeneous ice nucleation events, with mineral dust acting as the despite the other mission days with synoptic cirrus showing generally heterogeneous freezing characteristics. Model simulations reveal that ice residual analysis cannot capture influence of earlier heterogeneous freezing events, where mineral dust acted as ice-nucleating particles (INPs). Heterogeneous ice nucleation depleted INPs from cirrus forming altitudes, creating favourable conditions for These earlier events depleted INPs at cloud-forming altitudes, enabling homogeneous freezing at the time of observations. This study modelled cirrus cloud properties based on measured Cirrus cloud properties were simulated using measured meteorological and acrosol conditions and compared simulated results with observed cloud structures. It is shown that modelling Results show that modeling the impact of prior nucleation events on the vertical distribution of mineral dust and humidity in the model is necessary to reproduce the observed cloud characteristics. Heterogeneous ice nucleation primarily had freezing played a role in removal of ice-nucleation the removal of active mineral dust from cloud-forming altitudes well before arriving at the measurement location, while having limited role in forming ice crystals shortly before the time of measurements. Model results

<u>Simulations</u> also show that small-scale wave activity <u>strongly significantly</u> influenced ice nucleation efficiency and <u>overall</u> cloud properties. <u>While Although</u> large-scale atmospheric dynamics typically dominate synoptic cirrus formation, they alone were insufficient to replicate the observed cloud characteristics.

¹Finnish Meteorological Institute, 00560 Helsinki, Finland

²Department of Physics, University of Helsinki, Helsinki, 00014, Finland

³Institute for Atmospheric and Earth System Research/Physics, University of Helsinki, Helsinki, 00014, Finland

⁴Cooperative Institute for Research in Environmental Sciences, University of Colorado, Boulder, Colorado 80309, USA

⁵Air Innova Research and Consulting, Boulder, CO 80305, USA

⁶Bay Area Environmental Research Institute, Moffett Field, CA 94035, USA

⁷Department of Technical Physics, University of Eastern Finland, 70211 Kuopio, Finland

1 Introduction

55

The 2021 IPCC report (Forster et al., 2021) highlights that clouds and aerosols remain one of the primary sources of uncertainty in the Earth's energy budget and our ability to predict future climate. The intricate interactions between these atmospheric components pose significant challenges for climate modelling, particularly because microphysical processes occur at small spatial scales that cannot be directly resolved in general circulation models (GCMs) (Burrows et al., 2022). As a result, parametrizations are necessary, requiring a delicate balance between simplicity, realism, computational stability, and efficiency (Boucher et al., 2013).

Another substantial source of uncertainty in cloud radiative effects arises from the large knowledge gaps regarding humidity, particularly ice supersaturated regions in the upper troposphere and lower stratosphere (UTLS), where in-situ cirrus clouds form. At present, information on the large-scale transport of humidity in the UTLS primarily comes from numerical weather prediction (NWP) models, such as the Integrated Forecasting System (IFS) developed by the European Centre for Medium-Range Weather Forecasts (ECMWF, 2016) and the ICOsahedral Non-hydrostatic model (ICON; Zängl et al., 2015; Seifert and Siewert, 2024), used by the German Weather Service. These NWP models rely heavily on observational data to maintain a realistic representation of atmospheric conditions. However, the scarcity of spatially and temporally resolved observations in the UTLS hinders their ability to accurately predict ice supersaturation (S_i).

Over the past few decades, several key measurement campaigns (e.g., Krämer et al., 2009; Voigt et al., 2017) e.g., Pan et al. (2010, START), Jensen et al. (2013b, MACPEX), Wendisch et al. (2016, ACRIDICON-CHUVA), Jensen et al. (2017, ATTREX,BAMS), Pan et al. (2017, have been conducted in the UTLS. These campaigns have shown that high S_i is more common than predicted by NWPs. Such

high S_i levels promote the formation of UTLS cirrus clouds, which form synoptically in the absence of convection. However, given the uncertainties surrounding S_i , the formation mechanisms and occurrence of these synoptically driven cirrus clouds remain poorly quantified.

Synoptic cirrus Ciorus clouds primarily form through two dominant mechanisms: heterogeneous and homogeneous freezing (Pruppacher and Klett, 1997). Heterogeneous ice nucleation occurs either via immersion freezing, where insoluble particles—commonly referred to as ice-nucleating particles (INPs)—are embedded in aqueous droplets and trigger freezing, or via deposition nucleation, where water vapour vapor directly deposits onto dry, insoluble particles and freezes. For immersion freezing to occur, the INPs have to be somewhat hydrophilic or acquire a water-soluble coating during atmospheric transport. Electron microscopy studies (e.g., Kojima et al., 2006; Cziczo et al., 2013; Twohy, 2014) of cirrus crystal residuals have found that a substantial fraction of these particles consist of uncoated mineral dust. As coatings on mineral dust tend to suppress their heterogeneous ice nucleation efficiency (shifting the nucleation threshold toward higher supersaturation), deposition nucleation is likely the prevailing formation mechanism in many cases. In contrast, homogeneous freezing occurs in the absence of INPs and takes place when aqueous solution droplets freeze at temperatures below the -38°C threshold for pure water and at high S_i .

Ice nucleation in cirrus clouds is strongly influenced shaped by the abundance of INPs, which regulate how efficiently ice-nucleating particles (INPs), which govern the efficiency with which heterogeneous ice nucleation can suppress homogeneous freezingand

activity. Heterogeneous ice nucleationactivates and removes a population of ice-nucleation-active INPs from altitudes where they originate and end up lower in altitude through sedimentation of ice crystals. Cirrus clouds formed predominantly through heterogeneous ice nucleation tend to have ice crystal concentrations closely tied to the availability of INPs. In contrast, cirrus formed via homogeneous freezingoften exhibit a much wider range of suppresses homogeneous freezing. In heterogeneous nucleation, INPs trigger ice formation and are subsequently removed from higher altitudes as ice crystals sediment, whereas homogeneous freezing, occurring without INPs, produces ice crystal concentrations, depending on that vary with environmental factors such as temperature and vertical velocity (Kärcher and Lohmann, 2002). Modeling studies have significantly advanced our grasp of these processes (e.g. Sassen and Benson, 2000; Kärcher and Lohmann, 2002; Spichtinger and Cziczo, 2010; Rolf et with efforts spanning a range of scales, from high-resolution Large Eddy Simulations (Sölch and Kärcher, 2010) to global models (Liu et al., 2012; Tully et al., 2022; Beer et al., 2024). Yet, despite these advances, accurately representing INPs remains challenging due to their scarcity (0.01 to 100 L⁻¹ at -30°C; DeMott et al. (2010)) and a lack of good aerosol-aware freezing parameterizations, underscoring the need for refined parameterizations and robust observational constraints (Burrows et al., 2022)

Currently, the determination of One key method for determining whether a cirrus cloud formed through heterogeneous or homogeneous freezing is typically inferred from ice residual analysis. This technique involves evaporating ice crystals collected from cirrus clouds and analyzing the residual particles to infer the presence and nature of INPs that may have initiated freezing (Froyd et al., 2019). Studies like Cziczo et al. (2013) have used this approach to identify mineral dust and other particles in cirrus residuals, providing valuable clues about the nucleation process. However, while this method provides valuable insights, it does not capture the processes leading to the observed state of the cirrus cloud. The objective of this study is to use the ice residual analysis offers insights into the particles involved, it cannot fully capture the dynamic processes—such as the competition between heterogeneous and homogeneous freezing or the influence of vertical velocity and temperature fluctuations—that led to the observed cloud state. This limitation highlights the need for complementary approaches that can simulate these processes in greater detail.

Large-eddy simulation (LES) models, such as UCLALES-SALSA large-eddy model (Tonttila et al., 2017) to illustrate (Tonttila et al., 2017)

provide a powerful tool to address this gap by resolving small-scale turbulence and microphysical interactions at resolutions down to tens of meters, capturing INP-driven processes that coarser models heavily parametrize. This capability is crucial for understanding the complexity of cirrus eloud formation that cannot be fully explained by formation beyond what ice residual analysis alone can reveal. This work focuses on a case of cirrus cloud case single case (part of a multi day campaign) of cirrus observed during the Midlatitude Cirrus Properties Experiment MACPEX campaign (Jensen et al., 2013b), which predominantly exhibited homogeneous freezing among the analysed ice crystals (Cziczo et al., 2013). This raises a key question: why did this particular cirrus cloud form primarily through homogeneous freezing?

2 Methods

110

115

2.1 MACPEX campaign

The MACPEX campaign conducted by NASA was an aircraft measurement campaign aimed at investigating cirrus cloud properties (Jensen et al., 2013b). The campaign took place between March and April 2011, involving multiple science flights with the NASA WB-57F science aircraft over the southern United States. A total of 14 science flights were conducted, focusing on synoptic and anvil cirrus clouds, resulting in over 18.5 hours of cirrus sampling. In addition to in-situ in situ measurements, remote-sensing observations were coordinated to target cirrus clouds along the flight paths.

2.2 Description of the instruments used in the analysis

Ice number concentration, size distribution and IWC was measured by several, and ice water content (IWC) were measured using a number of in situ instruments. The two-dimensional stereo (2D-S; Lawson et al., 2006) probe is an optical imaging system which uses two pairs of probes to shoot. Two-Dimensional Stereo (2D-S) probe (Lawson et al., 2006) captures shadow images of ice particles using orthogonal laser beams to 128-photodiode arrays. Passing objects create a shadow which is observed on the sensors (Lawson et al., 2006). The 2D-S is capable of detecting particles with sizes and photodiode arrays. It 100 detects particles from 10 μ m to over 1 mm in diameter which is a good range for capturing the evolution of the crystal sizes in ice clouds. The 2D-S determines the crystal size and habit by using algorithm described in Lawson (2011) and results in filtration of biased data created by shattering crystals. The data for the very first, making it suitable for characterizing ice crystals in cirrus clouds. Due to known overestimations in the smallest size bin $(5-15-5-15 \mu m)$ of the 2D-S instrument is excluded in the analysis due to known over-estimations of the number concentrations, and this has been addressed in multiple studies, these data were excluded from the analysis (e.g., Jensen et al., 2013b; Krämer et al., 2016). The limited reliable observation capability 105 of 2D-S also includes filtering techniques to mitigate crystal shattering artifacts (Lawson, 2011). While the 2D-S probe above 15 μm restricts obtaining accurate information about young cirrus clouds with high number concentrations of smaller-sized particles (Krämer et al., 2016) can estimate IWC, its limitations, particularly with smaller particles can affect the accuracy of those estimates.

Meteorological variables For more precise measurements of ice water content (IWC), we use data from the University of Colorado closed-path tunable diode laser hygrometer (CLH) (Davis et al., 2007). The instrument measures enhanced total water by collecting both water vapor and sublimated ice particles via a subisokinetic inlet. Ice particles are evaporated in a heated absorption cell, and the resulting water vapor is quantified using a tunable diode laser. IWC is then derived by subtracting ambient water vapor and combining with meteorological data such as temperature , and pressure. Meteorological parameters, including temperature, pressure, winddirection and speed, geographic location, and speed of the aircraft were measured with, and aircraft motion, were obtained from the Meteorological Measurement System (MMS; Scott et al., 1990). The MMS vertical wind component measurements are filtered by subtracting 20 or 150 second (approximately corresponding to the model domain width (MMS) (Scott et al., 1990). MMS vertical velocity measurements were filtered to isolate fluctuations relevant to model-scale and mesoscale dynamics) local mean trend of wind from the using 20 Hz measurements. Additionally

vertical wind measurements from constant altitude legs are limited to a domain constrained by aircraft vertical velocity values below +/- and 150 second running means. Only data from constant-altitude flight legs with vertical aircraft speeds below ±1m/sin magnitude. The humidity was measured with multiple instruments, with the Harvard water vapour m s⁻¹ were used in the vertical wind analysis. Humidity was measured by several instruments; in this study, the Harvard Water Vapor (HWV) instrument being employed in this study, was used. Combined with MMS temperature, HWV data enables calculation of supersaturation over ice (S_i), a key indicator of ice nucleation conditions.

The NOAA Particle Analysis by Laser Mass Spectrometry (PALMS; Thomson et al., 2000; Froyd et al., 2019) instrument measures the Spectrometr instrument (PALMS; Thomson et al., 2000; Froyd et al., 2019) provides real-time, size-resolved chemical composition of particles in real time within the size range of aerosol particles in the 0.15to-5.0–5 μm (Thomson et al., 2000; Cziczo et al., 2013). The instrument operates by directing sample air into a vacuum system where an excimer laser ablates and ionizes the particles. The ionized particles are then analysed with a time of flight mass spectrometer (Murphy et al., 2006), and through post-processing, the particles can be classified based on their composition (Froyd et al., 2009). To obtain particle type-resolved number size distributions, the PALMS measurements were combined with those obtained from a focused cavity aerosol spectrometer (FCAS II; Jonsson et al., 1995). The FCAS II measures the size resolved particle number concentration within a measurable size-range. Combined with data from the Focused Cavity Aerosol Spectrometer (FCAS II; Jonsson et al., 1995) which provides aerosol measurements from size range of 0.07 to 1.5 μm. Initially, the particles pass through an anisokinetic sampler, which slows them down, and then they are transported to a laser cavity. Inside the cavity, the particlestraverse a laser beam, and , the scattering light is measured to determine their size (Jonsson et al., 1995). PALMS instrument enables classification of aerosol types and determination of particle-type-resolved number distributions (Froyd et al., 2019), providing both information of in-cloud (ice residual particles) and clear-air aerosol properties. These measurements are crucial for assessing the abundance and chemical composition of INPs relevant for cirrus cloud formation.

130

135

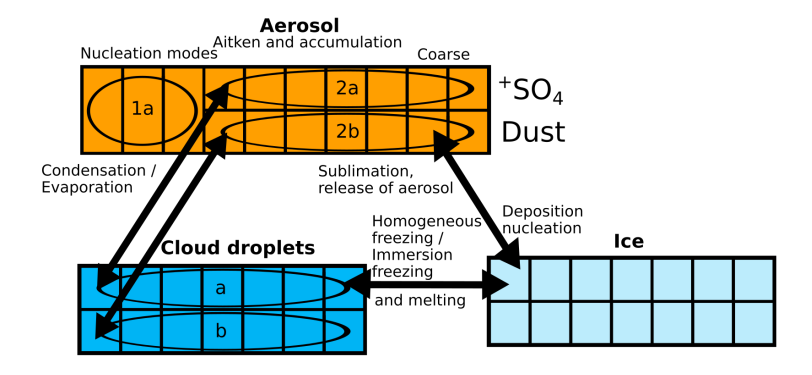


Figure 1. Bin scheme used in UCLALES-SALSA to track particle types relevant to ice nucleation in synoptic cirrus clouds. Freezing of rain is also possible while it is not shown here as it generally does not occur within the realms of this study.

2.3 UCLALES-SALSA

155

160

165

UCLALES-SALSA (Tonttila et al., 2017) is a large eddy (LES) model with a combination of sectional aerosol bin microphysics model SALSA (Sectional Aerosol module for Large-Scale Applications) (Kokkola et al., 2008; Tonttila et al., 2017; Kokkola et al., 2018). UCLALES is a well known atmospheric LES model based on the work (Stevens et al., 1999, 2005) of Stevens et al. (1999, 2005). The SALSA module enables tracking of four types of particles (including aerosols, cloud droplets, rain/drizzle particles and ice), and their particle size and chemical composition in a bin scheme, shown in Fig. 1. The aerosols are categorized into two distinct bins: one range, from 1a to 2a, addresses particles ranging from nucleation to coarse modes (3 nm — 10 μm), while the other, bin 2b, encompasses sizes above the Aitken and accumulation mode (50 nm — 10 μm). Particles falling within subrange 1a (3 — 50 nm) typically originate from new particle formation (e.g., sulfates) and may include some primary organic particles (Kokkola et al., 2008). This binning strategy enables separate tracking of two aerosol populations with an example: 2a for soluble sulfates crucial in cloud activation, and 2b for mineral dust particles relevant to ice nucleation. Furthermore, this parallel tracking extends to cloud and ice bins, facilitating comparison between the evolution of these two aerosol populations.

SALSA supports both heterogeneous and homogeneous freezing mechanisms. Of known heterogeneous freezing mechanisms, immersion, contact Ahola et al. (2020) implemented various freezing mechanisms, however, in this study, mainly homogeneous freezing and deposition nucleation have been implemented. Immersion freezing can occur when an aqueous solution droplet has an insoluble core such as mineral dust or black carbon. Contact freezing does not have a separate implementation in SALSA and is included in the immersion freezing scheme. Deposition nucleation can occur only for dry insoluble uncoated particles above supersaturated condition over ice $(S_i > 1)$, however, below saturation over water, are turned on as the typical temperatures within upper tropospheric cirrus clouds are below -38°C where pure water does not stay in liquid state. By default, UCLALES-SALSA uses homogeneous and heterogeneous ice nucleation parametrization schemes based on Khvorostyanov and Curry (2001), however, due to the heterogeneous ice nucleation schemes being stochastic (time dependent), it was concluded that ice nucleation could be greatly over-estimated in this particular study. To overcome this issue, a deterministic, time-independent deposition nucleation parametrization developed by Ullrich et al. (2017) for uncoated mineral dust particles was implemented to SALSA. This parametrization was created by using a fit to ice nucleation activity of several mineral dust particles presented in Kanji et al. (2011). For this scheme, tracking of activated INP fractions is necessary since deterministic parametrizations base their ice nucleation activity on original INP population. Homogeneous freezing is implemented based on the temperature and S_i relation presented in (Koop et al., 2000).

As illustrated in Fig.1, once ice-nucleation-active aerosols nucleate ice, they are removed from the aerosol bins and transferred to the ice bins. Within these ice bins, ice crystals can either grow or shrink through vapour depositionor evaporation, and they are sorted into their respective size bins. When the Once ice nucleation occurs, ice crystals are transferred from aerosol bins to ice crystals evaporate, the INPs are returned to the aerosol bins. The microphysics governing ice crystal vapour growth is based on Jacobson (2005). bins, where their subsequent evolution is governed by microphysical processes such as vapor deposition, sublimation, and sedimentation. The growth and evaporation of ice crystals are calculated using the framework from

Jacobson (2005). Ice sedimentation is explicitly resolved based on size-dependent terminal velocities. Additionally, ice-ice collisions are aggregation, influencing the size distribution of ice crystals over time. To represent ice crystal size distributions, the ice bins in SALSA range from 2 μm to 400 microns in diameter, ensuring a comprehensive resolution of both small ice crystals and larger particles. Ice crystals below 40 μm are assumed to be spherical, while those above this threshold are treated as bullet rosettes, following the habit-dependent parameterization in Baum et al. (2005). The habit transition is consistent with in situ cirrus observations that show a prevalence of bullet rosettes in larger particle size ranges. The ability to track the evolution of ice particle sizes is crucial in simulations of cirrus clouds, where the competition between heterogeneous and homogeneous freezing determines cloud properties. The sectional approach in SALSA allows for an accurate representation of ice nucleation pathways, growth dynamics, and size-dependent sedimentation, which are essential for understanding cirrus cloud evolution.

3 Case study-16 April 2011

185

190

200

205

A mission flight with the NASA WB-57F was flown on 16th of April to target cirrus cloud trail flowing easterly. The plane took off at 1700 UTC from Houston, Texas, and flew directly towards the cirrus clouds. Before flying into the cirrus clouds, lower stratospheric air was sampled and also provided the meteorological conditions over the cirrus cloud layers. The sampling of cirrus was done by flying back and forth following the cirrus cloud trail. The flight path is presented in Fig. 2.

3.1 Meteorological background

On April 16, 2011, the meteorological conditions over the Southwest Continental United States and Northern Mexico were characterized by the dominance of multiple high-pressure systems. Additionally, a cold front was associated with a low-pressure system in the Eastern United States, and its trailing edge extended over the Gulf of Mexico. Cloud top and bottom altitude derived from GOES-16 measurements along the flight altitude plotted against the time. Filtering was applied to the cloud top and bottom data due to the high uncertainty in data. The data with small uncertainty is connected with lines to illustrate better the approximate cloud top and bottom heights.

Meanwhile, a long trail of patchy cirrus clouds were forming over the Northern parts of Mexico and flowing easterly towards the Gulf of Mexico. According to ECMWF ERA5 reanalysis (Hersbach, 2023) data, these cirrus clouds formed in a moisture rich layer (10-12 km) originating from the Pacific Ocean, carried by a subtropical jet.

Figure ?? shows a derived product of cirrus cloud top and bottom altitudes, based Based on measurements from the Geostationary Operational Environmental Satellite-16 (GOES-16), operated by the National Oceanic and Atmospheric Administration (NOAA), correlated to the location of the WB-57F aircraft, where 2 km thick cirrus cloud layers between 10 and 12 km along the flight path can be seenwere identified. Figure 3 presents the vertical profile of meteorological variables during aircraft ascents and descents in the proximity of cirrus clouds. As the satellite retrieval suggests, the direct measurements show a layer of cirrus clouds with presence of high supersaturation over ice (S_i) between 10 and 12.5 km. This layer is called as supersaturated

layer from now on. The vertical layer where the cirrus clouds are present is stable throughout as the potential temperature gradient is significantly above 0 ($\frac{d\theta}{dz} > 0$). This implies that the formation of these cirrus clouds is influenced by large-scale forcing, classifying them as synoptic cirrus clouds . The supersaturation over ice (S_i) within the altitudes of cirrus clouds exhibits notable variability. As depicted in Fig. ??, the ascends and descents do not always intersect cloudy regions, indicating that the humidity data in Fig. 3 represents a mixture of clear air and cloudy air conditions. (e.g. Jensen et al., 2013b). Bright cirrus clouds around 8 UTC with temperatures below -40 °C. Temperature corresponds to the effective cloud top temperature of the clouds. Imagery taken with GOES-16 satellite. The center is marked with cross which indicates a location of an airparcel at 8 UTC which is traced to the location of WB-57F measurement later in time. The measured humidity inside the supersaturated layer varies significantly, indicating that vertical wind fluctuations might have a large influence on the humidity inside the cloud. Also, the ECMWF ERA5 reanalysis shows a significant spread in values for S_i along the WB-57F flight path. Most of the observed The S_i data points fall within the range of values provided by ERA5. However, S_i is almost entirely below 1-in the ERA5 data, indicating that cirrus cloud formation is under-represented in the reanalysis. This under-representation is further confirmed by the low values of cloud ice water mixing ratio along the flight path in the ERA5 datasetis an average over a grid box of approximately 28×28 km, meaning that a significant portion of variability is lost, while the overall levels of S_i is the same.

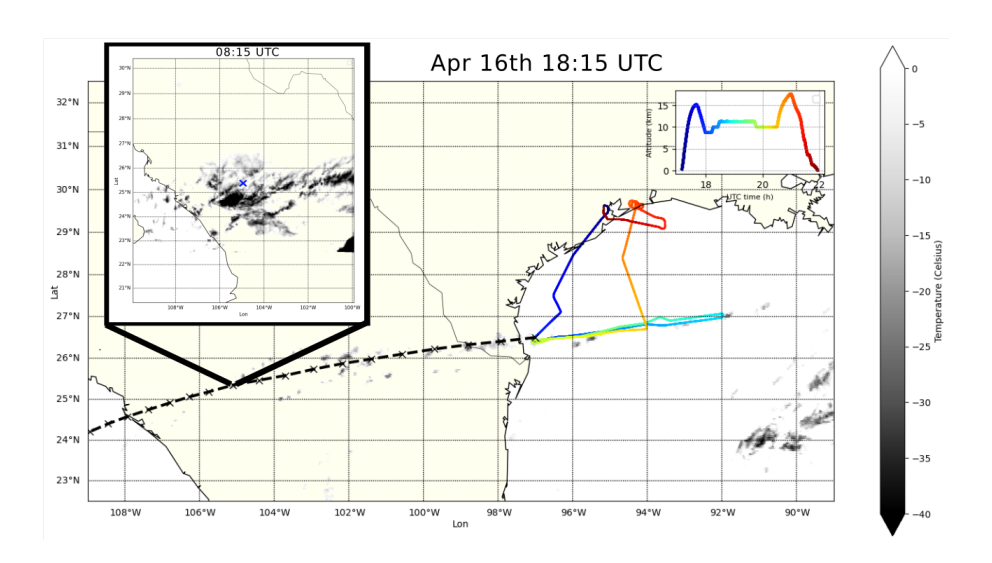


Figure 2. Flight GOES-16 satellite imagery shows infrared radiation (IR) temperature of cirrus cloud tops for 8.15 UTC (top-left focused panel) and 18.15 UTC (base). A back-trace trajectory trajectory with black dashed line and cross marking at every hour is shown, starting from the aircraft's intersection with the cirrus clouds at 18 UTC. The 8.15 UTC imagery with effective cloud-top temperatures below -40°C indicates intense cirrus clouds. A blue cross is marked in the centre of this panel to indicate where the air parcel was located around 8 UTC in the back-trace trajectory. The flight path of the WB-57F on April 1616th, 2011shown, is overlaid with coloured lines representing the aircraft's position. The colour of line on the map correlates the geographical position of the aircraft flight path corresponds to the altitude and time in UTC.

The formation mechanism of cirrus clouds is investigated through back-trajectory calculations conducted with Lagrangian analysis python script, utilizing wind field data from ERA5. As illustrated in Fig. 4, air parcels originating at 10 km appear to undergo major uplift around 4-7-4-7 UTC, influenced by topography interacting with the prevailing air-mass over the Western parts of Mexico with mountainous terrain. This uplifting is connected to the rapid development of high ice water content cirrus clouds, as evidenced by cold cloud temperatures in satellite imagery in the region as shown in Fig. ???2. The presence of mountain ranges induces gravity waves (Smith, 1979; Jensen et al., 1998; Joos et al., 2008, 2009), generating local ascending and descending air patterns downstream from the point of disturbance, even present during the time of WB-57F measurements over the ocean (between 18-20.5-18-20.5 UTC in Fig.4). The data shown strongly suggests that the cirrus cloud formation was induced by these gravity waves with periods of couple hours.

225

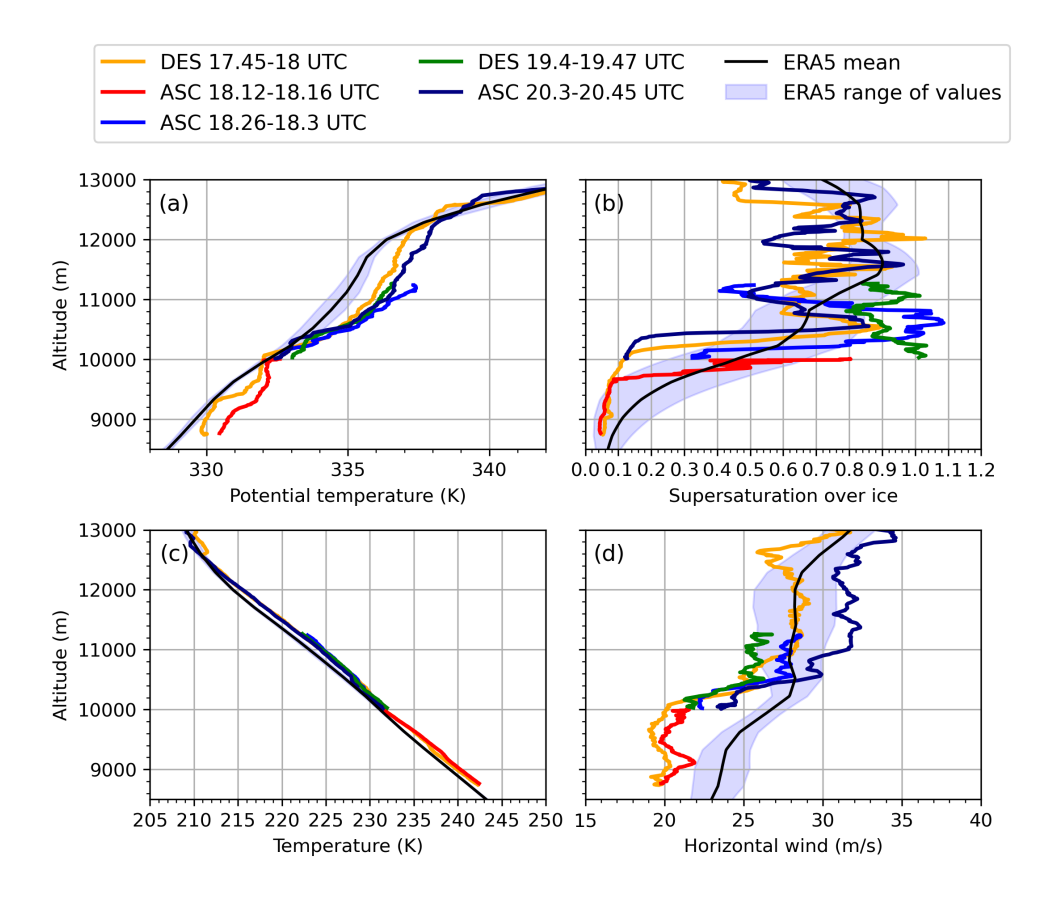
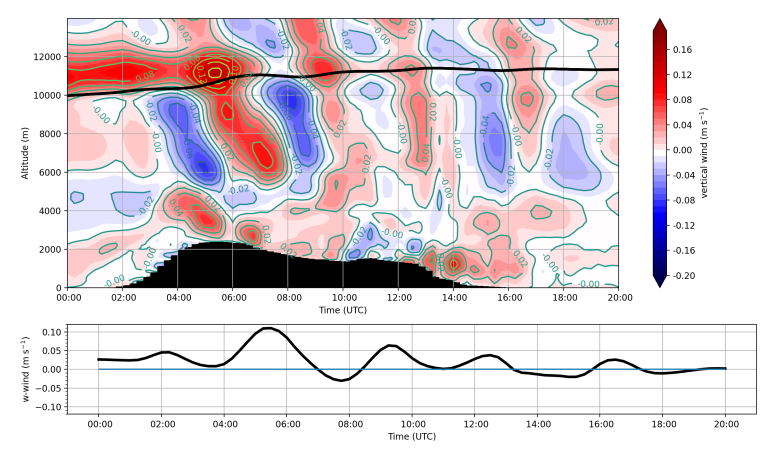


Figure 3. Potential temperature (a) , Potential temperature, (b) temperature, supersaturation over ice (c) supersaturation over ice and horizontal wind (d) horizontal wind measured with MMS during the ascents and descents of the aircraft. The vertical profiles are result of multiple multiple ascents (ASC) and descent (DES) through the cirrus cloud altutudes. ECMWF ERA5 data is shown with shading of light blue representing the $\frac{1}{2} - \sigma$ around the mean of altitude. Both MMS and 2DS observations are 1Hz data.



Vertical profile of vertical wind along the back-trajectory

analysis moving along the cirrus layer. Black line shows the movement of air parcel starting at 10 km at 0 UTC. The surface elevation is in black. The vertical wind around the air-parcel is shown in the lower panel

Figure 4. Vertical profile of vertical wind along the back-trajectory analysis moving along the cirrus layer. Black line shows the movement of air parcel starting at 10 km at 0 UTC. The surface elevation directly below the trajectory is in black. The vertical wind around the air-parcel is shown in the lower panel.

3.1 Indication of homogeneous freezing

235

245

The April 16th cirrus case was the only observed instance during the MACPEX campaign where the primary nucleation mechanism was predominantly homogeneous freezing (Cziczo et al., 2013). This conclusion is supported by examining the ice residual particle (IRP) populations—(Fig. 5). Particles composed of a mix of sulfates, organics, nitrates, and biomass burning particles contain a substantial fraction of water-soluble compounds (Reid et al., 2005), which promote homogeneous nucleation at temperatures below 235 K (Koop et al., 2000). In contrast, high IRP fractions of mineral dust and metallic particles are generally indicative of heterogeneous nucleation (Cziczo et al., 2013). Observations from April 16th revealed substantial fractions of sulfate/organic/nitrate particles (38%) and biomass burning particles in (39%) in the IRP, with a much lower fraction of mineral dust (10%) compared to heterogeneously nucleated cirrus cases presented by Cziczo et al. (2013) (see their Fig. 6). Interestingly, mineral dust fractions were higher in the observed IRP compared to clear-air aerosol fractions (Fig. 5), suggesting limited influence of mineral dust on the ice crystal population. This indicates that at least some ice likely formed heterogeneously, albeit not predominantly.

Cziczo et al. (2013) noted that mineral dust and metallic particles, when acting as heterogeneous INPs in cirrus clouds, are typically thinly coated, making them effective for deposition nucleation. However, PALMS spectral analysis showed that sulfate coatings on April 16th were thicker than on other MACPEX flight days (analysis results available in the supplementary material). Although the data quality is limited, this suggests that well-aged UTLS air results in thicker coatings on mineral dust particles, which may suppress their heterogeneous ice nucleation ability, as has been shown in previous studies (e.g., Cziczo et al., 2009; Eastwood et al., 2009; Chernoff and Bertram, 2010; Sullivan et al., 2010).

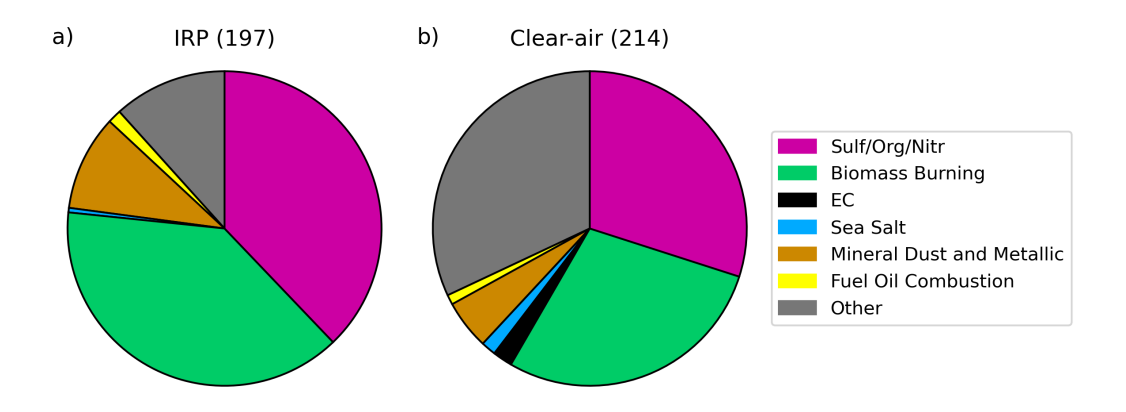


Figure 5. Lee cloud residual (a) Lee cloud residual and elear-air (b) clear-air contribution of aerosol species in a range from 0.2 to 3μ m for IRP and 0.2 to 1.5μ m for clear air.

of heterogeneous INP. These accounted for approximately one-third of the clear-air aerosol population, a greater proportion than observed during other MACPEX flights. These particles were compositionally typical of the region, with carbon-rich spectra inconsistent with sulfate/organic mixtures, and included some with pyridinium signatures.

There are some limitations to the analysis of IRP and clear-air particle compositions in this study. By definition, the measured clear-air aerosols are those that did not nucleate into ice at the time of measurement. Alternatively, these aerosols may have been involved in ice nucleation events and subsequent cloud sublimation well before the measurements were taken. Consequently, it is unclear whether these aerosols exhibit the same ice nucleation properties as those measured inside the cloud (IRP). Furthermore, the mineral dust particle fractions are averaged from a very limited clear-air sample set, making direct comparisons with IRP challenging. Additionally, the IRP data is inherently biased toward smaller ice crystals, which could potentially skew the results toward higher fractions of homogeneous IRP. However, clear-air particle fractions on Apr 16 were similar to the regional MACPEX averages.

The clear-air measured mineral dust concentration on April 16th in the upper troposphere (with lower stratospheric air filtration) was 2.05×10^{-2} cm⁻³. These values are slightly lower than the MACPEX campaign average (3.36×10^{-2} cm⁻³), however, in line with expected range of values in low latitude Northern hemisphere measured during ATom campaigns presented in Froyd et al. (2022).

260

In Fig. 6a, the measured N_i is presented and it despite the absence of measurements below 15 μ m exceeds the concentration of mineral dust particles or other potential heterogeneous INPs, providing strong evidence that homogeneous freezing played a significant role in shaping the N_i distribution. Homogeneous freezing typically requires S_i levels within the range of 1.46–1.54

at temperatures between 210 and 230 K (calculated with Eq. 10 in Ren and Mackenzie (2005)). The MMS-measured S_i in Fig. 6b reveals a notable absence of S_i values above 1.2, however, the measurements mostly represent either environment in the absence of clouds or inside matured cirrus clouds where the high S_i would be difficult to find. Observing high S_i required for homogeneous freezing is inherently challenging, especially within fully developed cirrus clouds, as the available humidity rapidly decreases following a homogeneous freezing event. This reduction is driven by nucleated ice crystals and sedimenting ice crystals from higher altitudes, which deplete the water vapour vapor within the layer. Numerical studies (e.g., Spichtinger and Cziczo, 2010) and in-situ in situ measurements (e.g., Jensen et al., 2013a) consistently show that S_i quickly returns to near-equilibrium levels after homogeneous freezing occurs, making it unlikely to detect significantly elevated S_i in measurements. These limitations highlight the difficulty of directly capturing the supersaturation levels required for homogeneous freezing in such environments.

3.2 Cloud vertical structure

270

275

285

290

295

300

Figure 6illustrates the distribution of N_i observed during the mission flight. A shift in the distribution of N_i measured with 2DS between two altitude levels is visible. The Nevertheless, the high levels of ice water content (IWC) observed within the cirrus clouds (Fig. 6c), occasionally coinciding with elevated S_i values—indicative of recent homogeneous freezing events (see supplementary Fig. S5)—support the hypothesis that these cirrus clouds most likely formed via homogeneous freezing (Krämer et al., 2016). Additionally, the median N_i is about an order of magnitude lower in the lower parts of cirruswhich could be explained by following factors: (a) Distribution of N₁ measured with 2DS inside cirrus clouds at two constant altitude levels with most continuous time series measured. Dashed line is drawn at the concentration of the mean clear-air concentration of mineral dust (0.0239 cm⁻³) by PALMS. (b) Supersaturation over ice measured at two constant altitude levels. Blue shading indicates homogeneous freezing threshold S₂ between 210-230 K based on equation presented in (Ren and Mackenzie, 2005). Homogeneous and heterogeneous ice nucleation produces higher number of ice when the temperatures are lower (Jensen et al., 2013b) , leading to higher N_i high and IWC low in the upper levels of cirrus, suggesting that the ice nucleation has occurred substantially in the upper parts of cirrus. The WB-57F collected statistically significant data between 9-11.2 km, covering only the lower portion of the cirrus cloud, where the supersaturated layer. The lack of high S_i is strongly influenced by in the lower parts of cirrus at 10 km can be explained by the large quantity of water vapor deposited on the sedimenting ice crystals. At 10 km, the formation of new ice crystals is more unlikely than at 11.2 km, as most ice at this altitude likely originated from higher layers. Competition for available water vapor further reduces the potential for ice nucleation. Another critical factor is the entrainment of ice crystals by dry pockets of air. As ice crystals traverse, they can enter layers of air that are subsaturated with respect to ice $(S_i < 1)$. In these subsaturated regions, some ice crystals sublimate, leading to a reduction in the N_i . This is more likely in the cirrus bottom altitudes (10 km) where the ice crystals have on average had a longer history. Finally, the vertical winds measured within the cirrus were of significantly higher magnitude than those typically associated with synoptic-scale motions, as shown in Fig.7. This suggests that S_i may have experienced considerable short-timescale variability, enabling the threshold for homogeneous freezing to be reached through strong upward motions. Figure 7 presents

the frequency distributions of observed vertical wind velocities during constant-altitude flight legs, with the vertical motions caused by aircraft ascents and descents and short scale systematic error filtered out.

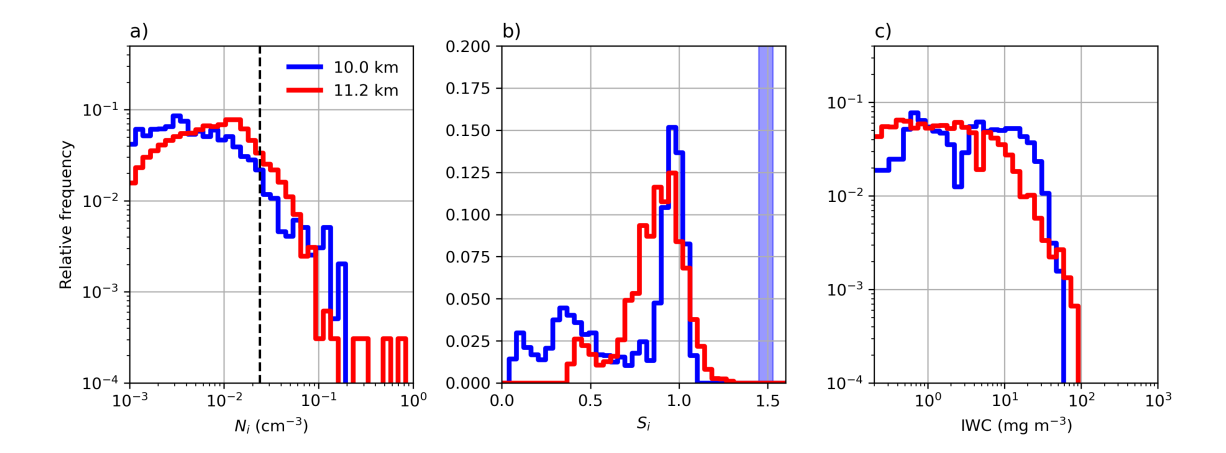


Figure 6. (a) Distribution of N_i measured with 2DS inside cirrus clouds at two constant altitude levels with most continuous time series measured. Dashed line is drawn at the concentration of the mean clear-air concentration of mineral dust $(2.05 \times 10^{-2} \text{ cm}^{-3})$ by PALMS-FCAS (b) Supersaturation over ice (S_i) measured at two constant altitude levels with HWV-MMS. Blue shading indicates homogeneous freezing threshold S_i between 210–230 K based on equation presented in (Ren and Mackenzie, 2005). (c) Ice water content (IWC) is from CLH measurements.

4 Model setup

3.1 Model setup

305

315

The UCLALES-SALSA simulations aim to attain results that closely align with measured data. The troposphere from the surface (0 km) to 14 km is simulated using a 3D domain to explore the impact of horizontal variability. The vertical resolution is set to $\Delta z = 300$ m below 6000 m·6 km and $\Delta z = 50$ m above 7000 m. Above 12500 m.7 km. Above 12.5 km, the vertical resolution is lowered linearly to $\Delta z = 300$ m. The resolution is linearly decreased between 6000 and 7000 m6 and 7 km. The vertical grid points are initialized by reading from file zm_grid_in. The time step is capped at a maximum of $\Delta t = 1$ s, which is suitable for simulating cloud microphysics. Data output is recorded at intervals of 5 minutes. The domain size spans 3×3 km with a horizontal resolution of $\Delta x = \Delta y = 50$ m in each direction. This resolution enables the simulation of small-scale eddies (Bryan et al., 2003). Additionally, sensitive tests are done by switching off ice nucleation processes and radiation scheme, and also running a 1D column simulations to examine horizontal variability free conditions. The meteorological variables used for the initial profile come from combined products of WB-57F measurements during the first descend towards the cirrus cloud layers before 18 UTC and the ERA5, shown in Fig. 8. The measurements made during this descend provides information from meteorological conditions throughout the cirrus clouds altitudes from 9 to 15 km. Data from ERA5 is used

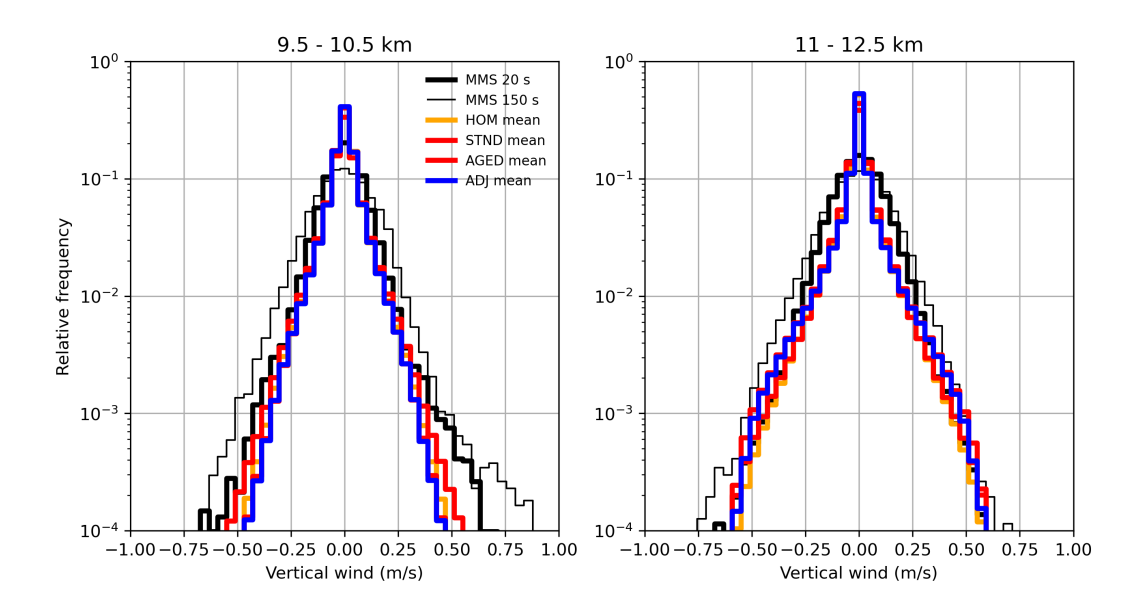


Figure 7. Frequency distribution of vertical wind in two altitudes for the MMS measured continuous statistical data with 20 and 150 second running mean filtering (black lines) and model data for all of the simulation set ups in (colored lines). The left panel represents a constant flight legs at altitude 10.0 km and the right panel at 11.2 km.

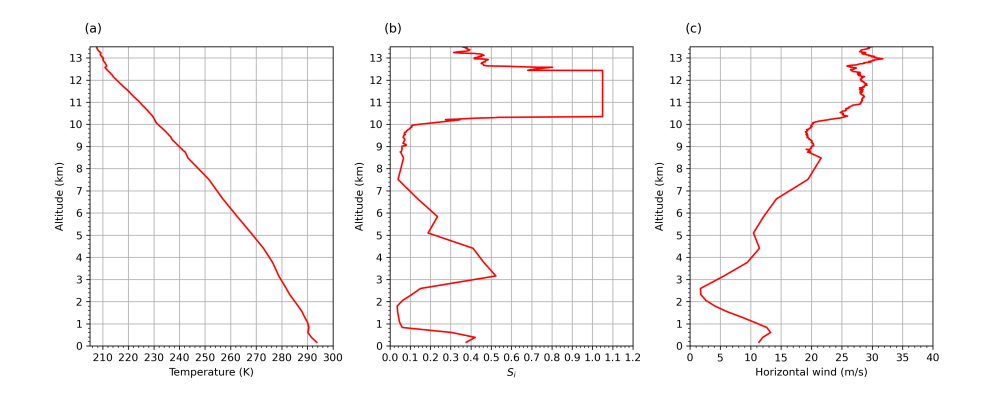


Figure 8. Initial profile temperature profiles of (a) temperature, S_i (b) supersaturation over ice and (c) horizontal wind used for in the simulations (e).

for the profile below 9 km as the aircraft did not descend below that altitude. It is, however, concluded that the lower resolution of the ERA5 is sufficient for lower altitudes as the dynamical effects of lower atmosphere has limited effect on the cirrus cloud layer as the atmosphere is relatively stable throughout. The stability within the cirrus cloud forming layer (hereby also known as supersaturated layer) supersaturated layer was relatively high and convection can not be expected. The temperature and humidity fields are perturbed with standard deviations of approximately $\sigma_{\theta} = 0.025$ K and $\sigma_{q} = 2 \cdot 10^{-6}$ kg /kgkg⁻¹.

These values are in the same order of magnitude to the values measured with WB-57F inside high humidity layers. The supersaturated layer with relatively high supersaturation over ice is set between 10 < z < 12.1 km. The initial S_i in these levels was the supersaturated layer between levels of 10 and 12.1 km is set to $S_i = 1.05$, approximately corresponding to the equilibrium humidity levels typically observed in fully matured cirrus clouds. Satellite imagery revealed that new cirrus clouds tended to form or intensify predominantly in regions where existing cirrus clouds were already present. This suggests that the mean atmospheric conditions in areas with sufficiently high S_i for cirrus formation were likely close to dynamic equilibrium. To simulate the effects of large-scale forcing observed in back-trajectory analysis, a constant updraught is applied to the model domain between altitudes of 3 km and 13 km. Constant updraught values of $w_{\rm LS} = 2,3,4,5$ cm s⁻¹ is used to simulate the effects of varying magnitude on the ice nucleation. After the model domain is lifted by 300 m, the ascent motion is halted. The 300 m lift corresponds to approximate maximum perturbation observed in the back-trajectory analysis. The lifting of the air leads to cooling with temperature rate rates given by the following equation: formulation:

325

330

335

340

345

350

355

$$\frac{dT}{dt} = \frac{dT}{dz}\frac{dz}{dt} = -\frac{g}{c_p}w_{\underline{LS}} = -\Gamma \cdot w_{\underline{LS}} \tag{1}$$

where Γ denotes the dry lapse rate (K km⁻¹), g and c_p denote the gravitational acceleration and the specific heat capacity for constant pressure. The cooling in turn increases the S_i as colder air has lower capacity to hold humidity. The initial choice of S_i significantly influences how high S_i can rise during a limited updraught duration. For instance, with a lapse rate of $\Gamma=10$ K $\rm Akmkm^{-1}$, the maximum cooling achieved with 300 m of lift corresponds to a temperature decrease of approximately 3 K. This, in turn, leads to an estimated increase in supersaturation of $\Delta S_i \approx 0.45$. The S_i levels after 300 m of lift correspond to level required for homogeneous freezing.

Additionally, the model domain experiences horizontal fluctuations in temperature, humidity and wind, and thus they are sensitive to more than the large scale forcing alone. For that, sensitivity runs are done without large scale forcing, radiation scheme and ice nucleation. Each simulation has 4 hour spin-up period where cloud microphysics and large scale forcing are disabled. The length of the spin-up was decided based on the relaxation of turbulent kinetic energy around 4 hours into the simulations. Ahola et al. (2020) implemented various freezing mechanisms, however, in this study, mainly homogeneous freezing and deposition nucleation are turned on as the typical temperatures within upper tropospheric cirrus clouds are below -38° where pure water does not stay in liquid state. By default, UCLALES-SALSA uses homogeneous and heterogeneous ice nucleation parametrization schemes based on Khvorostyanov and Curry (2000), however, due to the heterogeneous ice nucleation schemes being stochastic (time dependent), it was concluded that ice nucleation could be greatly over-estimated in this particular study. To overcome this issue, a deterministic, time-independent deposition nucleation parametrization developed by Ullrich et al. (2017) for uncoated mineral dust particles was implemented to SALSA. The reparametrization was created by using a fit to ice nucleation activity of several mineral dust particles presented in Kanji et al. (2011). For this scheme, tracking of activated INP fractions is necessary since deterministic parametrizations base their ice nucleation activity on original INP population. Homogeneous freezing is implemented based on the temperature and S_i relation presented in (Koop et al., 2000). The aerosol profiles for insoluble and soluble aerosols are derived from FCAS II and PALMS measurements. The analysis of the data was done using the method described in Froyd et al. (2019). In this case study, mineral dust is treated as the only insoluble aerosol particle or heterogeneous INP, while other insoluble aerosols were possibly present in aerosol population such as soot from biomass burning (34%) were excluded from heterogeneous INP population. Large number of sulfates, organics and nitrates (26%) were present in the aerosol population, particles which most likely act as INPs in homogeneous freezing. The measured mineral dust concentration on April 16 in the upper troposphere (with lower stratospheric air filtration) was 2.39×10^{-2} cm⁻³. These values are slightly lower than the MACPEX campaign average, however, in line with expected range of values in low latitude Northern hemisphere measured during ATom campaigns presented in Froyd et al. (2022). Additionally, this concentration is within the critical concentration for the heterogeneous ice nucleation to dominate over homogeneous freezing as reported in previous studies (Gierens, 2003; Spichtinger and Gierens, 2009). The The UCLALES-SALSA is run with two different concentrations of mineral dust: at the measured concentration (2.05×10⁻² cm⁻³) and at a reduced concentrationsconcentration, corresponding to 0.1 of the measured concentration (presented in Table 2). The reduced concentration represents a case where the mineral dust has lower INP activity due to coating, or has been scavenged by previous cirrus formation events. These runs are referred to as STND (standard) and AGED respectively from hereafter.

365

370

375

On the other hand, the rest of aerosols measured the observed aerosols (sulfate/organic/nitrate, biomass burning and other particles) are treated as soluble sulfate particles (H_2SO_4) and they are allocated to a-bins which potentially nucleate via homogeneous freezing from aqueous soluble droplets. The concentration of sulfates is set at constant $\frac{33.1 \times 10^{-2}}{34.9}$ cm⁻³ based on the measured values for sulfates, organics, and other aerosolFCAS mission average total concentration. The aerosols of both a- and b-bins a- and b-bins are distributed into four modes of log normal distributions and the parameters are shown in Table 1. Other possible insoluble aerosol such as black carbon are not included in the simulations. Notice that most of the soluble aerosols acting in homogeneous freezing are not measured by PALMS-FCAS due to the residual analysis restricted to aerosols above $0.2 \, \mu \text{m}$. The FCAS concentration (total aerosol) includes a large number of aerosols most likely acting as cloud condensation nuclei required for homogeneous freezing but also a small but insignificant fraction of heterogeneous INPs. Also the homogeneous freezing is known to be mostly insensitive to the concentration or size distribution of available aerosols unless the concentration is very low (Kärcher and Lohmann, 2002; Jensen et al., 2010) and thus the use of campaign average of soluble aerosols is justifiable. Once ice nucleation occurs in SALSA, ice crystals grow via a vapour deposition scheme

	$D_{g,1}$	σ_1	$N_{t,1}$	$D_{g,2}$	σ_2	$N_{t,2}$	$D_{g,3}$	σ_3	$N_{t,3}$	$D_{g,4}$	σ_4	$N_{t,4}$
Sulfates	0.118	1.19	27.3	0.183	1.3	5.76	0.444	1.29	0.049	0.722	1.13	0.010
Mineral dust	0.207	1.3	0.0178	0.222	1.04	0.363	0.476	1.09	0.0033	0.737	1.13	0.0003

Table 1. Parameters of the four log normal distributions (geometric geometric mean diameter D_g , geometric standard deviation σ and mode total number concentration N_t in cm⁻³).

according to formulation by Jacobson (2005). The ice crystal bins represent ice crystal mass sizes ranging from 2 to 500 μ m. For processes such as sedimentation, condensation, and coagulation, only ice-related particle processes are modelled, with an exception on condensation of water vapour on aerosol particles to enable homogeneous freezing. Ice crystals are assumed to be spherical for sizes below 40 μ m and bullet rosettes for larger particles. The habit dependence on size roughly follows the

suggestion by Baum et al. (2005), which indicates that ice crystals below 60 μ m are droxtals, while larger particles exhibit more complex habits. Images captured with the 2DS instrument during the April 16th flight show that a significant portion of larger ice crystals were bullet rosettes. To include the habit dependence on the crystal size, modification to mass transfer parametrizations were made. The capacitance was modified to reflect the increase in complexity of the ice crystal habit for larger crystals:

$$C_i(D_i) = \begin{cases} 0.5D_i, D_i < 40\mu m \\ 0.25D_i, D_i \ge 40\mu m \end{cases}$$

385

390 , where *D_i* is the diameter maximum size of an ice crystal. Additionally, the ice crystal shape parameters (mass-diameter and area-diameter relationship parameters) were modified to accommodate the habit dependency by crystal size and are given in Table ??. SALSA calculates terminal velocity of ice crystals by the formulation described in Mitchell and Heymsfield (2005) (previous versions of SALSA use the Khvorostyanov and Curry (2002) formulation).

Setup	œ Dust profile	β-Ice nucleation mechanisms	$\frac{\gamma \sigma}{\sigma}$ Humidity profile		
Spherical STND	$\frac{\pi}{6}\rho_{p}$ const. 2.05×10^{-2} cm ⁻³	3-het and hom	$\frac{\pi}{4}$ $S_i = 1.05$		
AGED	$\frac{2}{\text{const.}} 2.05 \times 10^{-3} \text{ cm}^{-3}$	$D_i < 40 \mu \text{ m}$ het and hom	$S_i = 1.05$		
Bullet rosette (5-sided) ADJ	0.0138 adjusted profile	2.26 het and hom	0.2148 adjusted profile		
HOM	1.7956 adjusted profile	$D_i \ge 40 \ \mu \ \text{m} \underbrace{\text{hom}}_{\text{c}}$	adjusted profile		

Table 2. Values for parameters in mass-diameter-Dust profile, ice nucleation mechanisms and area-diameter relationshipshumidity profile used in model run setups. The relationship between mass-Information regarding adjusted setups ADI and diameter is given as $m = \alpha D_i^{\beta}$ HOM are explained in Sect. The projected area and diameter relationship is given as $A = \gamma D_i^{\sigma} 4.3$.

In addition, the existing vapor mass flux equation inside SALSA was modified to include the mass accommodation coefficient for water vapor uptake of ice crystals (α_c) and it is set at $\alpha_c = 0.5$ for this case study. This value has a large uncertainty currently with measurements showing values in range $0.004 \ge \alpha_c \ge 1.06$ (see, Skrotzki et al., 2013). By default the α_c was practically set at 1 previously (with no parameter described), however, this value falls in the high end of the typically observed values.

4 Comparison of simulation data to observations

4.1 The effect of aged mineral dust on ice nucleation activity

In Fig. 9, the time evolution of a cirrus cloud deck produced with constant updraughts of $w_{LS} = 2 - 5$ cm s⁻¹ is shown for two simulation set ups STND (runs with PALMS concentration of mineral dust) and AGED (runs influenced by ageing of mineral dust), of which we focus first on the STND cases (left panels). The cirrus cloud initially forms in upper parts of the supersaturated layer, above 11 km, due to the high efficiency of heterogeneous ice nucleation at colder temperatures. Ice nucleation also becomes efficient in the lower parts of the supersaturated layer (below 11km) as temperatures continue to drop

and S_i increases. Once the constant updraught ceases, new ice crystal formation largely subsides. This happens due to the nature of the deterministic freezing parametrization used in this study, which does not allow further ice nucleation in constant S_i and warming temperatures. The the STND runs (Fig. 9, upper panels), the combination of heterogeneous ice nucleation and vapour vapor deposition growth of ice crystals effectively suppresses the increase in S_i , preventing it from reaching the levels required for homogeneous freezing. Even with an updraught updraft of $w_{LS} = 5$ cm cm s⁻¹ in Fig. 9)g(Fig. 9d), where growing ice crystals have less time to consume water vapourvapor, the suppression is remains strong enough to inhibit homogeneous freezing. This indicates that the measured mineral dust concentration is sufficiently high to prevent competition between homogeneous and heterogeneous ice nucleation mechanisms. If the constant updraught had continued for a longerperiodupdraft had persisted longer, homogeneous freezing could have occurred due to the depletion of available mineral dust particles in the supersaturated layer. However, back-trajectories suggested suggest that the maximum continuous large scale shifts of supersaturated layer was not sufficient-large-scale shifts of the supersaturated layer were insufficient for this to occurreases, the activation of mineral

405

410

The large-scale forcing (w_{LS}) also influences N_i indirectly. When w_{LS} increases, the activation of mineral dust is more efficient becomes more efficient, and the S_i suppression is weaker due to ice crystals having weakens because ice crystals have less time to consume water vapour vapor, resulting in higher N_i within a relatively short time frame. Conversely, in cases of slower updraughts updrafts, the activation process is more gradual, leading to lower N_i overall overall N_i .

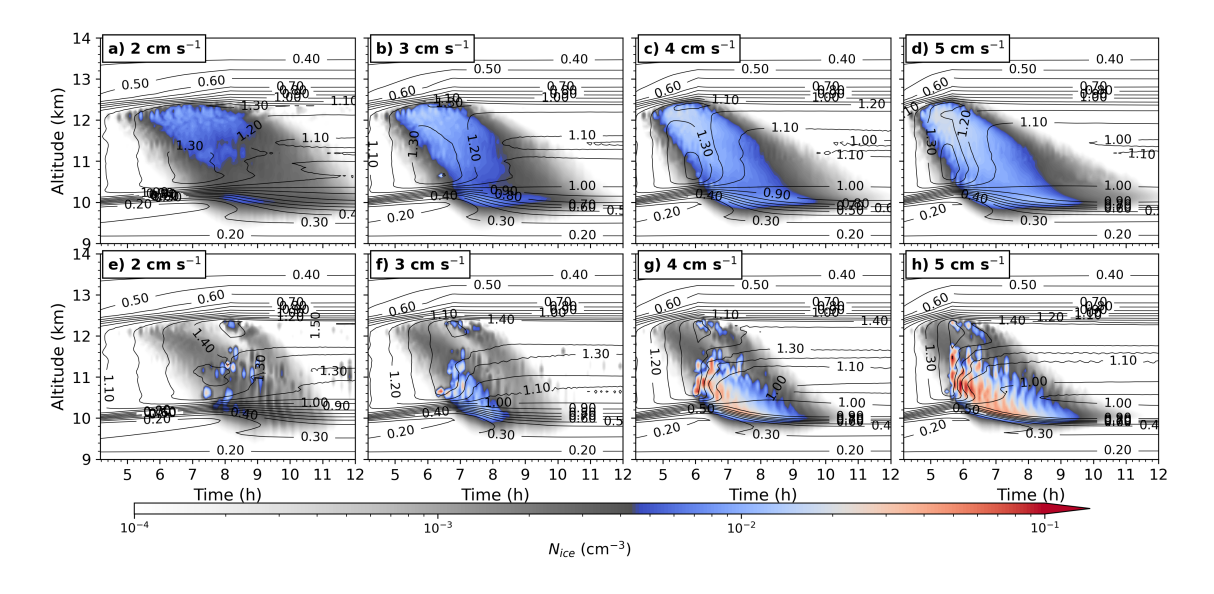


Figure 9. Cirrus clouds simulated with $w_{LS} = 2 - 5$ cm s⁻¹ for measured mineral dust concentrations (STND; a,e,e,ga-d) and reduced mineral dust concentrations (AGED; b,d,f,he-h). Black contour lines represent S_i at 0.1 intervals. The eolour color map highlights N_i at critical concentration levels relevant to this study: blue shades correspond to values typically associated with heterogeneous ice nucleation, while red shades indicate concentrations consistent with homogeneous freezing. Grey shades separate blue values from red, as the analysis focuses on high N_i levels in blue and red ranges. The profiles show a 1D vertical slice at the edge of the model domain, with S_i contours representing horizontal averages to reduce noise from horizontal fluctuations.

Looking at Examining the AGED cases (right lower panels in Fig. 9), initially, only a few ice crystals are produced as the due to the low number of ice-nucleation-active mineral dust particlesis low. The suppression of Si by the these few heterogeneous ice crystals growing is not sufficient and homogeneous freezingoceurs. In Fig. 9 right panels, the is insufficient, leading to homogeneous freezing. The occurrence of homogeneous freezing is noticeable from high evident from the steep gradient of Nias the homogeneous freezing, as it occurs only when the critical Si for homogeneous freezing is reachedand produces producing a large number of ice all at oncecrystals simultaneously. Interestingly, homogeneous freezing occurred at two distinct altitude ranges: between 10.5–11.8 km and within a narrow layer around 12 km. This is evident from the sharp gradient in Ni shown in Fig. 9. Near the top of the cirrus cloud (around 12.5 km), homogeneous freezing is facilitated by the fact that heterogeneous ice crystals deplete less water vapourvapor, leaving more available humidity compared to the lower layers, where larger ice crystals have grown and consumed more moisture. In the 10.5–11.8 km range, sufficient amplitude fluctuations in Si can occasionally push supersaturation beyond the threshold required for homogeneous freezing, even in the presence of heterogeneous ice. This phenomenon is discussed further in Section 5.45.1.1.

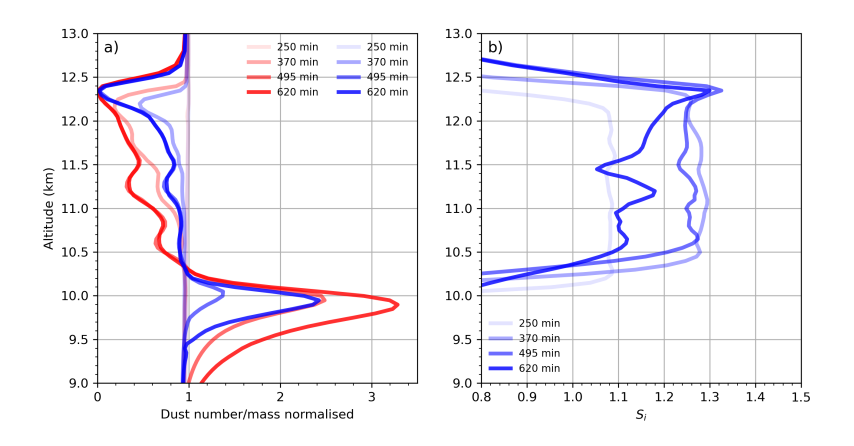


Figure 10. Time series of (a) the mineral dust number/mass (blue/red solid lines respectively) concentration (a) and S_i profiles (b) ice saturation profiles from the beginning to the end of the simulation using the STND setup. The mineral dust data is presented as normalized dust number/mass, expressed as a fraction of the initial values.

A notable pattern emerges from the model simulations, as shown in Fig. 10a, where mineral dust particles are depleted in both number and mass due to heterogeneous ice nucleation. The most efficient removal of dust occurs between 12 and 12.5 km, where only a small fraction of mineral dust particles remains by the end of the simulation. Below 12 km, a significant difference is observed between the depletion of dust number concentration and mass concentration, with mass being more heavily depleted. This discrepancy is largely attributed to the preferential activation of larger INPs, which possess greater surface areas and more active ice-nucleating sites, as described by the Ullrich et al. (2017) parameterization.

435

In contrast, the total number of dust particles remains relatively unaffected compared to the total mass, as the activated particles

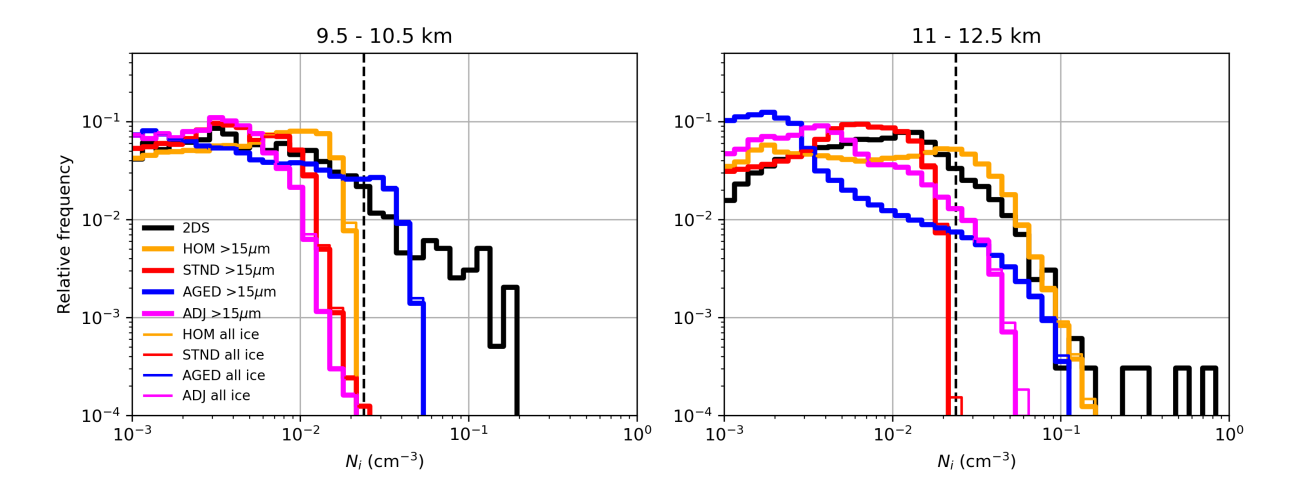


Figure 11. Distribution of N_i in two altitudes that the WB-57F measured continuous statistical data. The measurement data is from 2DS instrument which is in solid black lines. The STND and AGED runs stand for standard with measured mineral dust concentration, AGED for mineral dust particles that have aged. ADJ stands for adjusted profile set up runs and HOM for homogeneous freezing only runs. PALMS-FCAS measured mineral dust concentration shown with black dashed vertical line at $\frac{2.392.05 \times 10^{-2}}{2.392.05 \times 10^{-2}}$ cm⁻³.

are predominantly larger dust particles. While these larger particles are less numerous, they play a critical role in ice nucleation under the temperature ranges considered in this study. Between 12 and 12.5 km, the activation of mineral dust particles appears to be less dependent on particle size, as temperatures are below 215 K. For the Ullrich et al. (2017) parameterization, the efficiency difference between particle sizes becomes more pronounced in the temperature range of 215–230 K.

The Figure 10a additionally shows that the activated mineral dust particles eventually sediment to altitudes below saturation over ice (Fig. 10b). As a consequence of cirrus formation, mineral dust particles and other INPs involved can be transported vertically significant distances.

445

450

455

These findings have important implications for interpreting the mineral dust concentration measured by PALMS-FCAS. The clear-air concentration and size distribution of mineral dust may reflect a state influenced by previous nucleation events that occurred before the measurements. Most of the dust measurements were taken at constant altitudes of 10 and 11.2 km, and are not necessarily representative of ice initiation, which for these clouds is at >12km. above 12 km as evident from Fig. 10a. While there may be a lack of larger dust particles at these altitudes, their contribution to the overall number concentration would be minimal, and thus not easily detectable.

Additionally, ice crystal vapour vapor growth plays a crucial role in controlling the vertical distribution of humidity as shown in right panel of Fig. 10b. As ice crystals grow and sediment through the supersaturated layer, they deplete the surrounding humidity. Consequently, the vertical distribution of S_i exhibit a distinct pattern: near the top of cirrus clouds, S_i remains significantly above saturation, while below, it approaches saturation. This occurs because the descending ice crystals progressively consume water vapour vapor during sedimentation.

Figure 11 presents the distribution of N_i at two different altitude levels based on 2DS measurements and model outputs . The

(both for ice crystals filtered above 15 μ m and for all sizes). In the analysis, the modeled N_i and the measured N_i can be directly compared, as the difference between the total modelled N_i and the filtered values for ice crystals above 15 μ m is minimal.

In the STND runs, the maximum N_i did not surpass exceed the mineral dust concentration with the STND runs, emphasizing that with, indicating that a substantial presence of mineral dust throughout the supersaturated layer, homogeneous freezingwould be suppressed. The similar effectively suppressed homogeneous freezing. Similar findings were reported in Spichtinger and Gierens (2009) where they by Spichtinger and Gierens (2009), who simulated ice nucleation using different concentration levels of heterogeneous INP under varying concentrations of heterogeneous INPs and found that heterogeneous ice nucleation dominates nucleation dominated at INP concentrations above $20 L^{-1}$ which is in this case study right below the measured concentration of dust

particles, which is comparable to the measured mineral dust concentration in this study.

In contrast, the AGED runs demonstrated that the N_i surpassed the PALMS measured frequently exceeded the PALMS-measured

mineral dust concentration. The In the lower cirrus layers, N_i values in the lower parts of the cirrus clouds show a relatively good agreement with the 2DS observations in the AGED runs was significantly higher than in STND, as homogeneous freezing produced high N_i throughout the supersaturated layer. However, in the upper levels at upper altitudes, a significant portion fraction of N_i is focused remained concentrated around 10^{-3} cm⁻³. Higher, suggesting that most of the ice crystal population at these levels originated from heterogeneous nucleation. At lower altitudes, homogeneous freezing occurred more frequently in the AGED case. This increase in homogeneous freezing can be attributed to high-frequency gravity waves, which generated rapid fluctuations in temperature and supersaturation, periodically pushing S_i above the homogeneous freezing threshold.

These small-scale perturbations played a crucial role in enhancing ice nucleation activity in the lower cirrus layers.

4.2 The effects of atmospheric fluctuations

465

490

The 3D simulations provided a detailed representation of atmospheric variability under the given meteorological conditions. Although the atmosphere within the supersaturated layer remained relatively stable and free from convection, small-scale wave structures resembling gravity waves developed within the model domain. These fluctuations in vertical velocity (w) (Fig. 12a) were primarily driven by vertical wind shear between altitudes of 10 and 12 km. The resulting wave activity caused noticeable variability in S_i , with fluctuations of approximately 0–2% throughout the supersaturated layer during the spin-up phase (at 4 hour mark in Fig. 12b). As the simulations progressed, the amplitude of w fluctuations increased, leading to larger variations in S_i and influencing the intensity of homogeneous freezing present in AGED runs.

To evaluate whether the observed gravity wave-like fluctuations were an artifact of the model domain configuration, a series of sensitivity tests were conducted by varying the horizontal resolution and the domain size in both the X and Y directions. These wave features persisted even in simulations with significantly larger domains, ruling out the possibility that they were predominantly standing waves amplified over time due to insufficient kinetic energy dispersion (Fig. S1). Adjusting the horizontal grid resolution revealed that while the scale of these waves changed slightly, increasing the grid spacing beyond $\Delta x = 100$ m notably reduced the presence of small-scale wave activity.

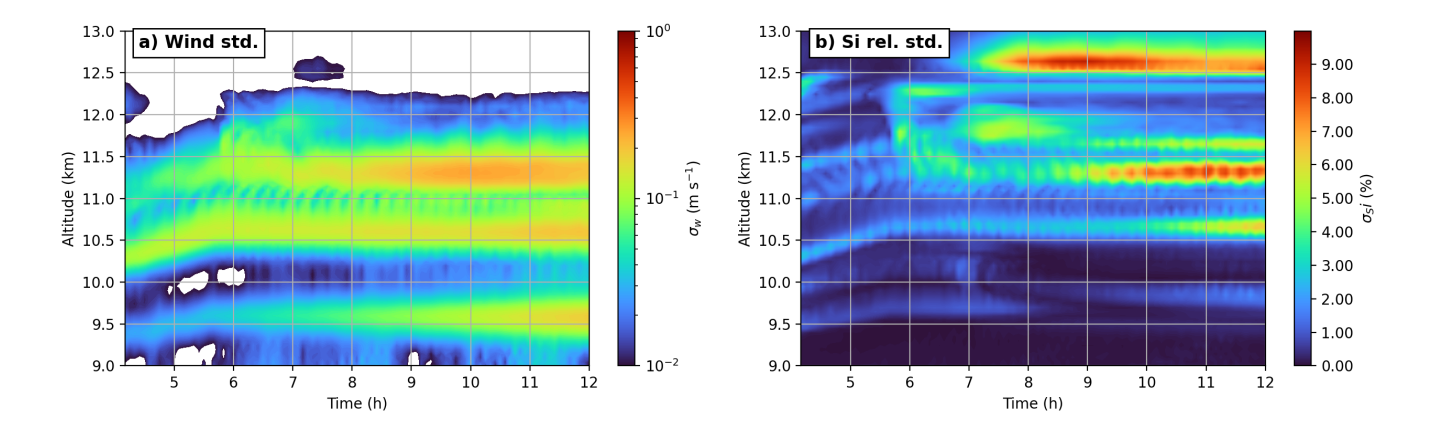


Figure 12. (a) Standard deviation of vertical wind and (b) relative standard deviation of supersaturation over ice S_i shown as shading inside a model domain at cirrus forming altitudes. The velocity fluctuations are generally the same for every set up of simulations used in this study. The variability for S_i was higher at the end of the model runs due to the ice nucleation and subsequent vapor growth of ice crystals affecting the distribution of S_i inside the model domain.

500

505

510

Figure 7 compares the simulated vertical wind velocity (w) with the MMS measurements filtered using a 20-second window. The resulting distributions show a strong resemblance, both exhibiting an ogival-shaped profile similar to that reported by Gierens et al. (2007). This similarity indicates that the model successfully captures vertical wind fluctuations at scales comparable to those observed in the real atmosphere. While the choice of ice nucleation mechanism in the model does introduce some differences between individual runs, the overall shape of the w distribution remains largely unaffected. The close agreement between the modeled and observed w distributions suggests that the simulated variability effectively mimics the wave activity occurring in the atmosphere. When the MMS w data is filtered using a 150-second window (Fig. 7), the distribution broadens slightly due to the inclusion of mesoscale wave motions with longer wavelengths—features that cannot fully develop within the 3×3 km model domain. Nevertheless, the range of MMS-observed w still aligns well with the modeled w, which is critical since the efficiency of homogeneous freezing is highly sensitive to vertical velocity magnitudes. To further assess the impact of vertical velocity fluctuations on the N_i values were predominantly generated by homogeneous freezing. At lower levels (9.5-10.5 km), homogeneous freezing seemed to generate higher distribution shown in Fig. 11, reference simulations were performed using a single-column setup, in which horizontal variability and wave activity are absent. As shown in Supplementary Fig. S9, these runs lack the high- N_i much more frequently. This increased homogeneous freezing in the lower parts of the cirrus clouds can be explained by the presence of high-frequency gravity waves in these layers, which provided the necessary conditions for more frequent nucleation events, tail observed in the 3D simulations, and the frequency of large N_i values is significantly reduced. These findings support the conclusion that gravity waves play a crucial role in shaping cirrus cloud microstructure, consistent with previous studies (Spichtinger and Gierens, 2009; Jensen et al., 2010; Kärcher et al., 2023) . The STND distribution, on the other hand, did not experience the influence from the fluctuations, mainly due to heterogeneous freezing being limited more by the relatively small concentration of INPs.

4.3 Accounting for prior cirrus formation

The previous runs

515

520

525

The previous simulations suggested that prior nucleation events likely removed a significant fraction of ice-nucleation-active mineral dust or and other INPs from the supersaturated layer (Fig. 10a). To explore this further further investigate this effect, additional simulations (referred to as ADJ runs) were conducted performed using adjusted dust and humidity profiles designed to approximate post-nucleation conditions, as shown in (Fig. 10for the dust profile.). The S_i profile was modified to reflect depletion of humidity following prior humidity depletion caused by earlier freezing events, resulting in leading to a peak S_i near the top of the supersaturated layer and reduced lower S_i below it at lower altitudes.

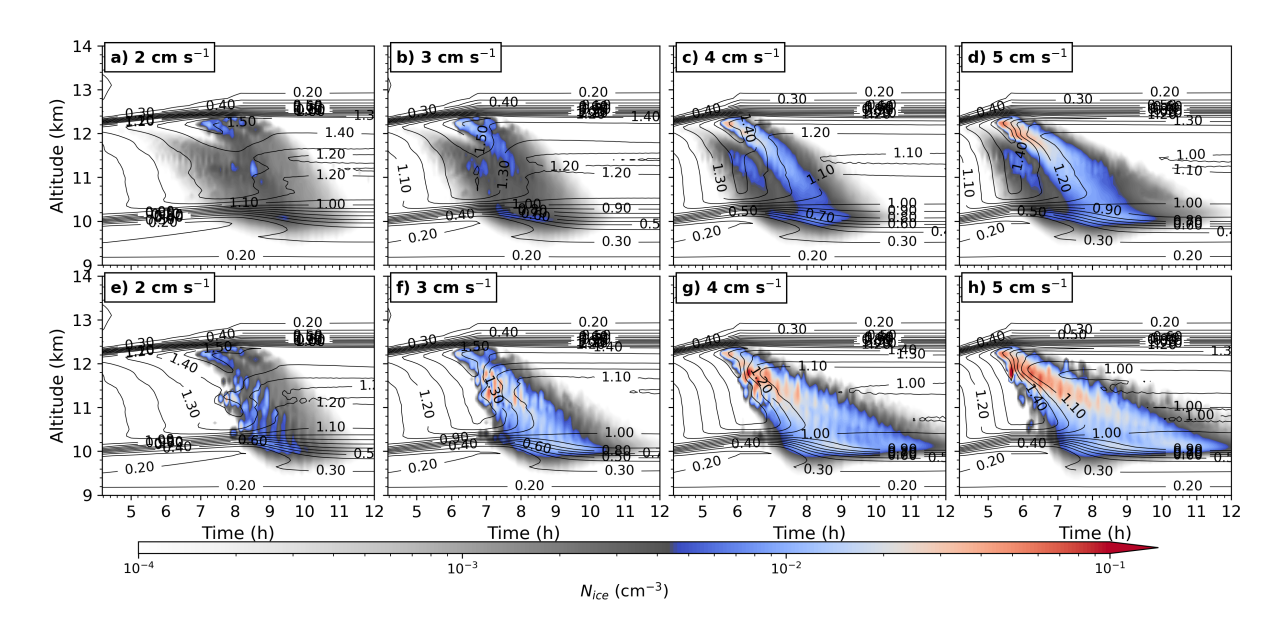


Figure 13. Cirrus clouds produced with $w_{LS} = 2 - 5$ cm s⁻¹ with adjusted mineral dust concentration and humidity ADJ (a-d) and only homogeneous freezing switched on HOM (e-h). The explanation of the details on the figure, see Fig.9.

Direct validation of the these elevated S_i values by using WB-57F measurements was not possible due to limited sampling, as—; the aircraft only recorded two passages—passed through the upper cirrus layers twice, leaving no continuous dataset. Likewise, validation of Similarly, validating the adjusted dust profiles was challenging , as the PALMS measurements were conducted at levels where the activation of mineral dust in absolute numbers proved to be not as efficient as in even higher altitudes. The measurements because PALMS-FCAS measurements were taken at altitudes where mineral dust activation was less efficient compared to even higher levels. Additionally, data near the top of the cirrus were absent, similarly was unavailable, similar to the humidity data. Neverthelessmeasurements. Despite these limitations, GOES-16 imagery (Fig. ??-2) and ERA5 back-trajectories (Fig4) indicate back-trajectory (Fig. 4) suggest that the air mass had undergone intense ice nucleation events before reaching the measurement locations ite. This supports the hypothesis that active dust particles were transported down-

ward, below the supersaturated layer, along with accompanying sedimenting ice crystals. Furthermore, there was no evidence of no evidence was found for significant horizontal mixing within the cirrus layer that could have reintroduced ice-nucleationactive dust particles into the supersaturated region.

535

540

545

550

555

560

Cirrus cloud produced with $w_{LS} = 2 - 5$ cm s⁻¹ with adjusted mineral dust concentration and humidity (a,c,e,g) and only homogeneous freezing switched on (b,d,f,h). The explanation of the details on the figure, see Fig.9. Figure 13 shows the Figure 13 presents the simulated cirrus clouds generated with the adjusted set up. Just as in using the adjusted setup. Similar to the AGED runs, the cirrus undergoes two distinct nucleation eventswhere significantly smaller number of ice is produced initially. The first occurs in the upper parts of cirrus (coloured in grey colors cloud layers, where only a small number of ice crystals form (represented by grey shades in Fig. 13left panels), followed by nucleation events where a large quantity of ice is produced at once by homogeneous freezing, upper panels). This is followed by a second, more intense nucleation event where homogeneous freezing produces a large number of ice crystals simultaneously.

Runs with heterogeneous ice nucleation To further explore the impact of prior heterogeneous nucleation, additional runs were conducted with heterogeneous freezing turned off (HOM; Fig. 13, right panels) and were conducted. These simulations serve as a reference case where the remaining majority of ice-nucleation-active mineral dust particles were largely absent from the supersaturated layer, likely had already been depleted during previous ice nucleation events where nucleation events when S_i had reached levels with high exceeded the threshold for efficient heterogeneous ice nucleation efficiency. The additional assumption is . It was assumed that the remaining mineral dust population is was fully activated, corresponding to a frozen fraction of 100%. The

In the HOM runs, homogeneous freezing occurred with 2-5 cm s⁻¹ updraught velocities around the time when S_i reaches eritical threshold S_i at all tested values of w_{LS} (Fig.13 right 13, lower panels). As there is no heterogeneous ice nucleation to suppress the In the absence of heterogeneous ice crystals to suppress S_i prior to homogeneous freezing, values of nucleation, the resulting N_i are at the highest possible out of all scenarios of model runs. Homogeneous freezing with high was the highest among all modeled scenarios. The large number of homogeneously nucleated ice crystals rapidly depleted the available water vapor, enabling the cirrus cloud to reach equilibrium conditions more quickly compared to the ADJ runs. Additionally, clear correlation is evident between N_i consumes efficiently humidity and the conditions inside cirrus clouds reach much faster the equilibrium state than and w_{LS} , with the highest N_i observed in the case of $w_{LS} = 5$ cm s⁻¹. This reflects the known sensitivity of homogeneous freezing to the magnitude of vertical velocity.

Returning to the discussion in Sect. 4.2, homogeneous freezing in both the ADJ and HOM runs—similarly to the AGED runs—was influenced by increased N_i within the cirrus. The high-end tail of the N_i distribution in the ADJ. Additionally, the lifetime of cirrus are extended slightly as the homogeneously frozen ice crystals grow to smaller sizes and sediment slower as the consumption of water vapour immediately after ice nucleation is significantly larger in quantity, and HOM simulations was extended in a manner comparable to that in the AGED cases. Notably, wave-induced fluctuations within the cirrus modulated the rate of homogeneous freezing between 10 and 12 km, where w fluctuations were most pronounced. In contrast, fluctuations were notably weaker between 12 and 12.5 km, where homogeneous freezing was almost entirely dependent on the imposed $w_{\rm LS}$. Consequently, the N_i values in both the ADJ and HOM runs could have been higher if stronger vertical wind fluctuations

had been present in the 12-12.5 km layer. Figure 13 supports this by showing that N_i was larger in the altitude regions where vertical velocity variability was greater.

4.4 Simulated ice crystal concentration suggests homogeneous freezing limited by initial heterogeneous ice nucleation

In the ADJ easesruns, the N_i exceed the dust concentration at least exceeds the mineral dust concentration, particularly in the upper parts of the cirrus at altitudes 11-12.5 km (cloud between 11 and 12.5 km altitudes (Fig. 11). This is primarily due to the low number of dust in the upper parts of the cirrus, enabling homogeneous freezing. There was a significant abundance of mineral dust at these altitudes, which allows supersaturation to rise and enables homogeneous freezing to occur. In contrast, a notable absence of high N_i is observed in the 9.5-10.5 km altitudes for ADJ campared -10.5 km range in the ADJ runs compared to AGED. This is mainly due to the difference can be attributed to the initially lower S_i being lower from the start and the lower parts of cirrus clouds and higher number in the adjusted humidity profile and a higher presence of mineral dust particlespresent, limiting the occurrence of homogeneous freezing. The high N_i in AGED cases at altitudes 9.5-10.5 km was a result from uniformly high S_i throughout the supersaturated layer, combined with low number of ice nucleation-active mineral dust particles. In Fig. 11, the homogeneously frozen N_i distribution is shown. It seems that the shape agrees relatively, both of which suppress homogeneous freezing in the lower cirrus layers.

Figure 11 also shows the distribution of N_i from homogeneous freezing. The shape of this distribution aligns reasonably well with the 2DS measurements, especially well at the high end of particularly at the higher end of the N_i . There is a slight lack of low N_i in the upper parts of cirrus and the high frequency is concentrated in the narrow range of values above the mean of measurements. Among all cases in this studyspectrum.

Among all the presented simulations, the HOM simulations show runs exhibit the closest statistical resemblance to agreement with the 2DS measurements, proving that without any influence of heterogeneous ice nucleation he. This suggests that in the absence of heterogeneous nucleation, homogeneous freezing can generate N_i exceed the clear air values that most effectively exceed the background concentration of mineral dustmost efficiently.

4.5 The effects of atmospheric fluctuations

570

575

580

585

590

595

The 3D simulations offered a comprehensive depiction of atmospheric variability in meteorological conditions. Despite relatively stable atmosphere within the supersaturated layer without presence of convection, small-scale waves resembling gravity waves emerged within the model domain. The vertical wind (w) in MMS measurements on April 16th and in model domain are shown together in Fig. 7. The w observed in the model domain stemmed from local instabilities arising from vertical wind shear at altitudes between 10 and 11 km. These waves induced notable fluctuations in S_i (as shown in Fig.??), with variability around 0-5% throughout supersaturated layer during the spin-up phase of the simulations. Frequency distribution of vertical wind in two altitudes for the MMS measured continuous statistical data with 20 and 150 second running mean filtering and model data for all of the simulation set ups. Sensitivity tests were done by adjusting the horizontal resolution, domain size in both X and Y directions. These waves were present even in larger domains excluding the possibility that these waves were predominantly standing waves that self-amplified over time. In the 9.5–10.5 km range, the AGED simulation matches the

observed N_i distribution most closely. This agreement is primarily due to the lack of kinetic energy dispersion inside the domain (Fig. S1). By changing the horizontal grid resolution, the size of these waves slightly changed, and increasing the grid size above $\Delta x=100$ m diminished the presence of these small scale waves significantly. Examining Fig. 7, it becomes evident that the measured MMS w filtered with 20-second filter, the distribution is very closed to simulated w distribution. The model and simulated w both exhibit an ogival-shaped distribution similar to one reported by Gierens et al. (2007). The similarity of the w distributions confirm that the modelled fluctuations are simulated correctly. The modelled ice nucleation mechanisms do not seem to affect significantly the shape of the distribution, however, some variation is visible between each model run. Overall, the relatively good agreement of distributions mean that the variability in the model domain emulates the wave activity inside real atmosphere. The 150-second filtered MMS w data (Fig. 7) broadened the distribution shape slightly as it includes more mesoscale waves of larger wavelengths that were not simulated inside 3 × 3 km model domain. The higher range of MMS w aligns well with the modelled w, which is crucial since homogeneous freezing efficiency is highly sensitive to these magnitudes of w. It was stated previously that the maximum N_i achieved in HOM cases was not clearly correlated to the imposed large-scale w. The cooling within the supersaturated layer was primarily influenced by the large-scale w; however, small-scale turbulence induced local variations in temperature and humidity. These fluctuations caused the initially high and uniform S_i to intermittently reach the critical level necessary for homogeneous freezing. While the large-scale w_{1S} ranged from $2 \text{ to } 5 \text{ cm s}^{-1}$, turbulent w fluctuated between $\pm 0.6 \text{ m/s}$ as seen in Fig. 7, frequently exceeding the magnitude of the large-scale w_{1.S}. The high frequency of turbulence resulted in high-profile and the relatively low abundance of heterogeneous ice-nucleating particles in that case. However, considering the evolution of humidity distributing after multiple nucleation events, a uniformly high S_i with short lifetimes as shown in example in Fig. ??. Sensitivity tests conducted using a single-column setup (results in Supplementary data S8) reveal that, in the absence of horizontal variability and turbulence, high N_i at the high tail end of distributions (in Fig. 11) are completely absent.

4.4.1 Practical examples of heterogeneous and homogeneous freezing cases

600

605

610

615

(a) Homogeneous freezing case from HOM run and (b) heterogeneous ice nucleation case from STND run. The plots show temperature (red), supersaturation over ice (Si, blue), and ice crystal number concentration (Ni, black) before and during freezing events. The critical supersaturation for homogeneous freezing, based on Eq. 10 in Ren and Mackenzie (2005), is indicated by dashed blue lines. The timing of the homogeneous freezing event is highlighted with gray shading. Figure ??a illustrates the meteorological variables immediately before and after the onset of homogeneous freezing with parcel trajectories.
625 The trajectory reveals a relationship between turbulent fluctuations, Si, and the Ni. It is evident that Si and temperature fluctuates apart from the general trend before the onset of homogeneous freezing, with these variations occurring over phase times significantly smaller than the imposed vertical velocity which represents the behaviour of larger scale gravity wave. As Si increases and approaches the critical threshold Si for homogeneous freezing, Ni rapidly reaches to peak levels. Immediately after a freezing event, the concentration starts to decrease quickly as the ice crystal fall out of the air parcel. Previous numerical studies (Jensen et al., 2010; Spichtinger and Krämer, 2013) have shown that the interaction between high-frequency gravity waves and slow, large-scale cooling can result in different ice concentrations compared to scenarios involving only large-scale

cooling. These interactions can lead to either higher or lower concentrations of ice crystals, depending on the phase of the gravity waves and the cooling rates profile at the start of the model runs is likely an unlikely representation of real atmospheric conditions at the time of homogeneous freezing. The homogeneous freezing event depicted in Fig. ?? represents a situation where the wave was in a cooling phase, resulting in a high-measurements. Such profiles would typically require vertically differential cooling rates (which was not evident in this case study from Fig. 4) and very small N_i that would not remove ice supersaturation. Figure ??b illustrates a case of heterogeneous ice nucleation. Each peak in S_i along the parcel's trajectory corresponds to an increase in N_i , as new ice crystals form during these supersaturationevents. However, after 1.5 hours into the simulation, this correlation becomes less evident due to the influence of sedimenting ice crystals, which alter the local ice crystal population. As the cooling phase ends, S_i begins to decline as the growing ice crystals deplete available water vapour. Concurrently, N_i decreases gradually as ice crystals sediment out of the layer, while additional crystals are introduced into the population from sedimentation originating in higher altitudes. The presence of these growing ice crystals effectively prevents S_i from reaching levels necessary for homogeneous freezing. This suppression becomes particularly pronounced around 1.5 hours into the simulation, as the ice crystals efficiently limit further increases in S_i .

645 5 Possible limitations of this study

635

640

650

655

660

In this study, only mineral dust particles were considered as INPs. However, other aerosol components, such as soot, glassy particles, and coated soluble droplets, may also contribute to the heterogeneous INP population and influence the overall ice nucleation activity in cirrus clouds. The ice nucleation efficiency of these additional INP types remains less well understood, and their inclusion in the model would introduce further uncertainties. Furthermore, the conclusions drawn from this study are constrained by the limited sample size of the measured aerosol particles and the restricted vertical sampling, which was conducted only between 10 and 11.2 km. As a result, this study cannot fully validate the simulation outcomes or confirm the robustness of its conclusions.

Furthermore, this study simulated cirrus cloud formation under specific conditions that allowed homogeneous freezing to occur in scenarios where the effects of heterogeneous ice nucleation were limited. If the model had been run under conditions unfavourable to homogeneous freezing, the results would have looked significantly different, with N_i primarily constrained by the number of heterogeneous INPs. While simulating cirrus with lower N_i might have increased the variability of cloud conditions, cirrus clouds with higher N_i would still have dominated the analysis, meaning the overall conclusions would not have been significantly affected.

In contrast, adjusting the initial humidity or increasing the vertical displacement of the supersaturated layer would have favoured more efficient homogeneous freezing. However, the main interpretation of this study remains unchanged. The behaviour of freezing in cirrus clouds—and the occurrence of homogeneous freezing—was shown to be highly dependent on the presence of heterogeneous INPs. Homogeneous freezing did not occur, regardless of the initial S_i or the magnitude of the vertical displacement, when the number of heterogeneous INPs at the cirrus cloud top matched the concentrations from the PALMS-PALMS-FCAS observed at lower levels.

665 6 Conclusions

670

680

685

690

Based on the observations from the MACPEX campaign, the top layer of cirrus clouds on April 16th, 2011, were predominantly formed through homogeneous freezing, as evidenced by ice residual particle (IRP) analysis. Other days of the MACPEX campaign with similar conditions showed that the heterogeneous ice was dominating the IRP analysis. We investigated the role of heterogeneous ice nucleation with the UCLALES-SALSA model, and the results showed that previous events with heterogeneous ice nucleation increases the likelihood of homogeneous freezing occurring during subsequent ice nucleation events. Simulations with measured mineral dust concentrations (STND) showed an almost complete absence of homogeneous freezing due to heterogeneous ice preventing supersaturation over ice from reaching the critical threshold level for homogeneous freezing. This suggests that prior heterogeneous nucleation events likely depleted the heterogeneous INPs from certain layers of the cirrus clouds, particularly in the colder upper regions . This depletion and indirectly enabled the conditions necessary for subsequent homogeneous freezing to occur.

Finally, vertical shear instabilities within the supersaturated layer led to turbulence and gravity waves, which in turn caused substantial variability in temperature and S_i . This wave activity resulted in greater variability in the N_i and the rate of homogeneous freezing compared to a scenario without such waves. Notably, the changes in temperature and S_i were slower for large-scale motions, highlighting the significant role of smaller-scale perturbations in affecting ice nucleation processes.

Although clear-air INP measurements were not available at cloud top altitudes, MACPEX dust concentrations typically had little vertical structure throughout the cirrus regime. For the Apr 16 case we assume that dust measured at mid- and low-cloud levels was representative of initial cloud top conditions. This underscores the need for improved measurements of aerosol populations, with high sample rate of INPs in both horizontal and vertical directions in future campaign. This study also demonstrated that high resolution three dimensional LES model studies are able to simulate huge variability of N_i inside cirrus that large scale relatively low resolution models simulating the global impacts of cirrus clouds struggle. The LES approach demonstrated that small scale gravity waves can be simulated without using a separate parameterization to simulate the effects of small scale gravity waves (Jensen et al., 2013a). In future, inclusion of more INPs to simulate cirrus clouds could clear uncertainties that were not explored in this study.

Code availability. The source code of the model UCLALES-SALSA is available from GitHub at https://github.com/UCLALES-SALSA/UCLALES-SALSA under release tag MACPEX_icenucl.

Data availability. The campaign data from the MACPEX field study, which was used in this study, is publicly available at the following URL: https://espoarchive.nasa.gov/archive/browse/macpex/WB57. UCLALES-SALSA model data for runs with single seed used for analysis archived at Zenodo (DOI:10.5281/zenodo.14500482. For whole dataset, contact the corresponding author.

Author contributions. KJ made the simulations, analysed the simulation results and wrote major parts of the text. CW contributed to experiment design, size distribution analysis, and provided input on the manuscript. KF provided detailed analysis of PALMS spectra, derived measured concentrations of aerosol components and guided with MACPEX campaign data. JD provided information on interpreting MMS instrument data and analysis of vertical wind data. AL supervised the project and provided input on the manuscript.

Competing interests. Some authors are members of the editorial board of Atmospheric Chemistry and Physics.

Acknowledgements. This work was supported by the Academy of Finland Flagship ACCC (grant no. 337552) and MEDICEN project (grant no. 345125 and 359892). Supercomputing resources were provided by CSC– IT Center for Science, Ltd., Finland. We thank J.C. Wilson for use of the FCAS aerosol data.

References

- Ahola, J., Korhonen, H., Tonttila, J., Romakkaniemi, S., Kokkola, H., and Raatikainen, T.: Modelling mixed-phase clouds with the large-eddy model UCLALES–SALSA, Atmospheric Chemistry and Physics, 20, 11 639–11 654, https://doi.org/10.5194/acp-20-11639-2020, 2020.
- Baum, B. A., Heymsfield, A. J., Yang, P., and Bedka, S. T.: Bulk Scattering Properties for the Remote Sensing of Ice Clouds. Part I: Microphysical Data and Models, Journal of Applied Meteorology, 44, 1885 1895, https://doi.org/10.1175/JAM2308.1, 2005.
 - Beer, E., Righi, M., Hendricks, J., and Tost, H.: Impacts of ice-nucleating particles on cirrus clouds and radiation derived from global model simulations with MADE3 in EMAC, Atmospheric Chemistry and Physics, 24, 3217–3245, https://doi.org/10.5194/acp-24-3217-2024, 2024.
- Boucher, O., Randall, D., Artaxo, P., Bretherton, C., Feingold, G., Forster, P., Kerminen, V.-M., Kondo, Y., Liao, H., Lohmann, U., Rasch, P., Satheesh, S. K., Sherwood, S., Stevens, B., and Zhang, X. Y.: Clouds and aerosols, pp. 571–657, Cambridge University Press, Cambridge, UK, https://doi.org/10.1017/CBO9781107415324.016, 2013.
 - Bryan, G. H., Wyngaard, J. C., and Fritsch, J. M.: Resolution Requirements for the Simulation of Deep Moist Convection, Monthly Weather Review, 131, 2394 2416, https://doi.org/10.1175/1520-0493(2003)131<2394:RRFTSO>2.0.CO;2, 2003.
- Parrows, S. M., McCluskey, C. S., Cornwell, G., Steinke, I., Zhang, K., Zhao, B., Zawadowicz, M., Raman, A., Kulkarni, G., China, S., Zelenyuk, A., and DeMott, P. J.: Ice-Nucleating Particles That Impact Clouds and Climate: Observational and Modeling Research Needs, Reviews of Geophysics, 60, e2021RG000745, https://doi.org/https://doi.org/10.1029/2021RG000745, 2022.
 - Chernoff, D. I. and Bertram, A. K.: Effects of sulfate coatings on the ice nucleation properties of a biological ice nucleus and several types of minerals, Journal of Geophysical Research: Atmospheres, 115, https://doi.org/https://doi.org/10.1029/2010JD014254, 2010.
- Cziczo, D. J., Froyd, K. D., Gallavardin, S. J., Moehler, O., Benz, S., Saathoff, H., and Murphy, D. M.: Deactivation of ice nuclei due to atmospherically relevant surface coatings, Environmental Research Letters, 4, 044 013, https://doi.org/10.1088/1748-9326/4/4/044013, 2009.
 - Cziczo, D. J., Froyd, K. D., Hoose, C., Jensen, E. J., Diao, M., Zondlo, M. A., Smith, J. B., Twohy, C. H., and Murphy, D. M.: Clarifying the Dominant Sources and Mechanisms of Cirrus Cloud Formation, Science, 340, 1320–1324, https://doi.org/10.1126/science.1234145, 2013.
 - Davis, S., Hallar, A., Avallone, L., and Engblom, W.: Measurement of Total Water with a Tunable Diode Laser Hygrometer: Inlet Analysis, Calibration Procedure, and Ice Water Content Determination, Journal of Atmospheric and Oceanic Technology, 24, 463–475, https://doi.org/10.1175/JTECH1975.1, 2007.
- DeMott, P. J., Prenni, A. J., Liu, X., Kreidenweis, S. M., Petters, M. D., Twohy, C. H., Richardson, M. S., Eidhammer, T., and Rogers, D. C.:
 Predicting global atmospheric ice nuclei distributions and their impacts on climate, Proceedings of the National Academy of Sciences,
 107, 11 217–11 222, https://doi.org/10.1073/pnas.0910818107, 2010.
 - Eastwood, M. L., Cremel, S., Wheeler, M., Murray, B. J., Girard, E., and Bertram, A. K.: Effects of sulfuric acid and ammonium sulfate coatings on the ice nucleation properties of kaolinite particles, Geophysical Research Letters, 36, https://doi.org/https://doi.org/10.1029/2008GL035997, 2009.
- Forster, P., Storelvmo, T., Armour, K., Collins, W., Dufresne, J.-L., Frame, D., Lunt, D., Mauritsen, T., Palmer, M., Watanabe, M., Wild, M., and Zhang, H.: The Earth's Energy Budget, Climate Feedbacks, and Climate Sensitivity, p. 923–1054, Cambridge University Press, Cambridge, United Kingdom and New York, NY, USA, https://doi.org/10.1017/9781009157896.009, 2021.

- Froyd, K., Yu, P., Schill, G., Brock, C., Kupc, A., Williamson, C., Jensen, E., Ray, E., Rosenlof, K., Bian, H., Darmenov, A., Colarco, P., Diskin, G., Bui, T., and Murphy, D.: Dominant role of mineral dust in cirrus cloud formation revealed by global-scale measurements,

 Nature Geoscience, 15, 1–7, https://doi.org/10.1038/s41561-022-00901-w, 2022.
 - Froyd, K. D., Murphy, D. M., Sanford, T. J., Thomson, D. S., Wilson, J. C., Pfister, L., and Lait, L.: Aerosol composition of the tropical upper troposphere, Atmospheric Chemistry and Physics, 9, 4363–4385, https://doi.org/10.5194/acp-9-4363-2009, 2009.
 - Froyd, K. D., Murphy, D. M., Brock, C. A., Campuzano-Jost, P., Dibb, J. E., Jimenez, J.-L., Kupc, A., Middlebrook, A. M., Schill, G. P., Thornhill, K. L., Williamson, C. J., Wilson, J. C., and Ziemba, L. D.: A new method to quantify mineral dust and other
- aerosol species from aircraft platforms using single-particle mass spectrometry, Atmospheric Measurement Techniques, 12, 6209–6239, https://doi.org/10.5194/amt-12-6209-2019, 2019.
 - Gierens, K.: On the transition between heterogeneous and homogeneous freezing, Atmospheric Chemistry and Physics, 3, 437–446, https://doi.org/10.5194/acp-3-437-2003, 2003.
- Gierens, K., Kohlhepp, R., Dotzek, N., and Smit, H. G.: Instantaneous fluctuations of temperature and moisture in the upper troposphere and tropopause region. Part 1: Probability densities and their variability, Meteorologische Zeitschrift, 16, 221–231, https://doi.org/10.1127/0941?2948/2007/0197, 2007.
 - Hersbach, H., B. B. B. P. B. G. H. A. M. S. J. N. J. P. C. R. R. R. I. S. D. S. A. S. C. D. D. T. J.-N.: ERA5 hourly data on pressure levels from 1940 to present. Copernicus Climate Change Service (C3S) Climate Data Store (CDS), https://doi.org/10.24381/cds.bd0915c6, 2023.
 - Jacobson, M. Z.: Fundamentals of Atmospheric Modeling, Cambridge University Press, 2 edn., 2005.
- Jensen, E. J., Toon, O. B., Tabazadeh, A., Sachse, G. W., Anderson, B. E., Chan, K. R., Twohy, C. W., Gandrud, B., Aulenbach, S. M., Heymsfield, A., Hallett, J., and Gary, B.: Ice nucleation processes in upper tropospheric wave-clouds observed during SUCCESS, Geophysical Research Letters, 25, 1363–1366, https://doi.org/https://doi.org/10.1029/98GL00299, 1998.
 - Jensen, E. J., Pfister, L., Bui, T.-P., Lawson, P., and Baumgardner, D.: Ice nucleation and cloud microphysical properties in tropical tropopause layer cirrus, Atmospheric Chemistry and Physics, 10, 1369–1384, https://doi.org/10.5194/acp-10-1369-2010, 2010.
- 760 Jensen, E. J., Diskin, G., Lawson, R. P., Lance, S., Bui, T. P., Hlavka, D., McGill, M., Pfister, L., Toon, O. B., and Gao, R.: Ice nucleation and dehydration in the Tropical Tropopause Layer, Proceedings of the National Academy of Sciences, 110, 2041–2046, https://doi.org/10.1073/pnas.1217104110, 2013a.
 - Jensen, E. J., Lawson, R. P., Bergman, J. W., Pfister, L., Bui, T. P., and Schmitt, C. G.: Physical processes controlling ice concentrations in synoptically forced, midlatitude cirrus, Journal of Geophysical Research: Atmospheres, 118, 5348–5360, https://doi.org/10.1002/jgrd.50421, 2013b.
 - Jensen, E. J., Pfister, L., Jordan, D. E., Bui, T. V., Ueyama, R., Singh, H. B., Thornberry, T. D., Rollins, A. W., Gao, R.-S., Fahey, D. W., Rosenlof, K. H., Elkins, J. W., Diskin, G. S., DiGangi, J. P., Lawson, R. P., Woods, S., Atlas, E. L., Rodriguez, M. A. N., Wofsy, S. C., Pittman, J., Bardeen, C. G., Toon, O. B., Kindel, B. C., Newman, P. A., McGill, M. J., Hlavka, D. L., Lait, L. R., Schoeberl, M. R., Bergman, J. W., Selkirk, H. B., Alexander, M. J., Kim, J.-E., Lim, B. H., Stutz, J., and Pfeilsticker, K.: The NASA Airborne Tropical
- 770 Tropopause Experiment: High-Altitude Aircraft Measurements in the Tropical Western Pacific, Bulletin of the American Meteorological Society, 98, 129 143, https://doi.org/10.1175/BAMS-D-14-00263.1, 2017.
 - Jonsson, H., Wilson, J., Brock, C., Knollenberg, R., Newton, T., Dye, J., Baumgardner, D., Borrmann, S., Ferry, G., Pueschel, R., Woods, D. C., and Pitts, M. C.: Performance of a Focused Cavity Aerosol Spectrometer for Measurements in the Stratosphere of Particle Size in the 0.06-2.0microm-Diameter Range, Journal of Atmospheric and Oceanic Technology, 12, 115–129,
- 775 https://doi.org/https://doi.org/10.1175/1520-0426(1995)012<0115:POAFCA>2.0.CO;2, 1995.

- Joos, H., Spichtinger, P., Lohmann, U., Gayet, J.-F., and Minikin, A.: Orographic cirrus in the global climate model ECHAM5, Journal of Geophysical Research: Atmospheres, 113, https://doi.org/https://doi.org/10.1029/2007JD009605, 2008.
- Joos, H., Spichtinger, P., and Lohmann, U.: Orographic cirrus in a future climate, Atmospheric Chemistry and Physics, 9, 7825–7845, https://doi.org/10.5194/acp-9-7825-2009, 2009.
- 780 Kanji, Z. A., DeMott, P. J., Möhler, O., and Abbatt, J. P. D.: Results from the University of Toronto continuous flow diffusion chamber at ICIS 2007: instrument intercomparison and ice onsets for different aerosol types, Atmospheric Chemistry and Physics, 11, 31–41, https://doi.org/10.5194/acp-11-31-2011, 2011.
 - Khvorostyanov, V. I. and Curry, J. A.: A new theory of heterogeneous ice nucleation for application in cloud and climate models, Geophysical Research Letters, 27, 4081–4084, https://doi.org/10.1029/1999GL011211, 2000.
- 785 Khvorostyanov, V. I. and Curry, J. A.: Terminal Velocities of Droplets and Crystals: Power Laws with Continuous Parameters over the Size Spectrum, Journal of the Atmospheric Sciences, 59, 1872 1884, https://doi.org/10.1175/1520-0469(2002)059<1872:TVODAC>2.0.CO;2, 2002.
 - Kojima, T., Buseck, P., Iwasaka, Y., Matsuki, A., and Trochkine, D.: Sulfate-coated dust particles in the free troposphere over Japan, Atmospheric Research, 82, 698–708, https://doi.org/10.1016/j.atmosres.2006.02.024, 2006.
- Kokkola, H., Korhonen, H., Lehtinen, K. E. J., Makkonen, R., Asmi, A., Järvenoja, S., Anttila, T., Partanen, A.-I., Kulmala, M., Järvinen, H., Laaksonen, A., and Kerminen, V.-M.: SALSA ndash; a Sectional Aerosol module for Large Scale Applications, Atmospheric Chemistry and Physics, 8, 2469–2483, https://doi.org/10.5194/acp-8-2469-2008, 2008.
 - Kokkola, H., Kühn, T., Laakso, A., Bergman, T., Lehtinen, K. E. J., Mielonen, T., Arola, A., Stadtler, S., Korhonen, H., Ferrachat, S., Lohmann, U., Neubauer, D., Tegen, I., Siegenthaler-Le Drian, C., Schultz, M. G., Bey, I., Stier, P., Daskalakis, N., Heald, C. L., and
- Romakkaniemi, S.: SALSA2.0: The sectional aerosol module of the aerosol–chemistry–climate model ECHAM6.3.0-HAM2.3-MOZ1.0, Geoscientific Model Development, 11, 3833–3863, https://doi.org/10.5194/gmd-11-3833-2018, 2018.
 - Koop, T., Luo, B., Tsias, A., and Peter, T.: Water Activity as the determinant for homogeneous ice nucleation in aqueous solutions, Nature, 406, 611–4, https://doi.org/10.1038/35020537, 2000.
- Krämer, M., Schiller, C., Afchine, A., Bauer, R., Gensch, I., Mangold, A., Schlicht, S., Spelten, N., Sitnikov, N., Borrmann, S., de Reus, M., and Spichtinger, P.: Ice supersaturations and cirrus cloud crystal numbers, Atmospheric Chemistry and Physics, 9, 3505–3522, https://doi.org/10.5194/acp-9-3505-2009, 2009.
 - Krämer, M., Rolf, C., Luebke, A., Afchine, A., Spelten, N., Costa, A., Meyer, J., Zöger, M., Smith, J., Herman, R. L., Buchholz, B., Ebert, V., Baumgardner, D., Borrmann, S., Klingebiel, M., and Avallone, L.: A microphysics guide to cirrus clouds Part 1: Cirrus types, Atmospheric Chemistry and Physics, 16, 3463–3483, https://doi.org/10.5194/acp-16-3463-2016, 2016.
- 805 Krämer, M., Rolf, C., Luebke, A., Afchine, A., Spelten, N., Costa, A., Meyer, J., Zöger, M., Smith, J., Herman, R. L., Buchholz, B., Ebert, V., Baumgardner, D., Borrmann, S., Klingebiel, M., and Avallone, L.: A microphysics guide to cirrus clouds Part 1: Cirrus types, Atmospheric Chemistry and Physics, 16, 3463–3483, https://doi.org/10.5194/acp-16-3463-2016, 2016.
 - Kärcher, B. and Lohmann, U.: A parameterization of cirrus cloud formation: Homogeneous freezing of supercooled aerosols, Journal of Geophysical Research: Atmospheres, 107, AAC 4–1–AAC 4–10, https://doi.org/https://doi.org/10.1029/2001JD000470, 2002.
- Kärcher, B., Jensen, E. J., and Lohmann, U.: The Impact of Mesoscale Gravity Waves on Homogeneous Ice Nucleation in Cirrus Clouds, Geophysical Research Letters, 46, 5556–5565, https://doi.org/https://doi.org/10.1029/2019GL082437, 2019.

- Kärcher, B., DeMott, P. J., Jensen, E. J., and Harrington, J. Y.: Studies on the Competition Between Homogeneous and Heterogeneous Ice Nucleation in Cirrus Formation, Journal of Geophysical Research: Atmospheres, 127, e2021JD035805, https://doi.org/https://doi.org/10.1029/2021JD035805, 2022.
- Kärcher, B., Jensen, E. J., Pokrifka, G. F., and Harrington, J. Y.: Ice Supersaturation Variability in Cirrus Clouds: Role of Vertical Wind Speeds and Deposition Coefficients, Journal of Geophysical Research: Atmospheres, 128, e2023JD039324, https://doi.org/https://doi.org/10.1029/2023JD039324, e2023JD039324 2023JD039324, 2023.
 - Lawson, R. P.: Effects of ice particles shattering on the 2D-S probe, Atmospheric Measurement Techniques, 4, 1361–1381, https://doi.org/10.5194/amt-4-1361-2011, 2011.
- Lawson, R. P., O'Connor, D., Zmarzly, P., Weaver, K., Baker, B., Mo, Q., and Jonsson, H.: The 2D-S (Stereo) Probe: Design and Preliminary Tests of a New Airborne, High-Speed, High-Resolution Particle Imaging Probe, Journal of Atmospheric and Oceanic Technology, 23, 1462 1477, https://doi.org/10.1175/JTECH1927.1, 2006.

- Liu, X., Shi, X.and Zhang, K. J. E. J., Gettelman, A., Barahona, D., Nenes, A., and Lawson, P.: Sensitivity studies of dust ice nuclei effect on cirrus clouds with the Community Atmosphere Model CAM5, Atmospheric Chemistry and Physics, 12, 12 061–12 079, https://doi.org/10.5194/acp-12-12061-2012, 2012.
- Mitchell, D. L. and Heymsfield, A. J.: Refinements in the Treatment of Ice Particle Terminal Velocities, Highlighting Aggregates, Journal of the Atmospheric Sciences, 62, 1637 1644, https://doi.org/10.1175/JAS3413.1, 2005.
- Murphy, D. M., Cziczo, D. J., Froyd, K. D., Hudson, P. K., Matthew, B. M., Middlebrook, A. M., Peltier, R. E., Sullivan, A., Thomson, D. S., and Weber, R. J.: Single-particle mass spectrometry of tropospheric aerosol particles, Journal of Geophysical Research: Atmospheres, 111, https://doi.org/10.1029/2006JD007340, 2006.
- Pan, L., Bowman, K., Atlas, E., Wofsy, S., Zhang, F., Bresch, J., Ridley, B., Pittman, J., Homeyer, C., Romashkin, P., and Cooper, W.: The stratosphere-troposphere analyses of regional transport 2008 experiment, Bulletin of the American Meteorological Society, 91, 327–342, https://doi.org/10.1175/2009BAMS2865.1, 2010.
- Pan, L. L., Atlas, E. L., Salawitch, R. J., Honomichl, S. B., Bresch, J. F., Randel, W. J., Apel, E. C., Hornbrook, R. S., Weinheimer, A. J.,
 Anderson, D. C., Andrews, S. J., Baidar, S., Beaton, S. P., Campos, T. L., Carpenter, L. J., Chen, D., Dix, B., Donets, V., Hall, S. R.,
 Hanisco, T. F., Homeyer, C. R., Huey, L. G., Jensen, J. B., Kaser, L., Kinnison, D. E., Koenig, T. K., Lamarque, J.-F., Liu, C., Luo, J.,
 Luo, Z. J., Montzka, D. D., Nicely, J. M., Pierce, R. B., Riemer, D. D., Robinson, T., Romashkin, P., Saiz-Lopez, A., Schauffler, S.,
 Shieh, O., Stell, M. H., Ullmann, K., Vaughan, G., Volkamer, R., and Wolfe, G.: The Convective Transport of Active Species in the
 Tropics (CONTRAST) Experiment, Bulletin of the American Meteorological Society, 98, 106 128, https://doi.org/10.1175/BAMS-D14-00272.1, 2017.
 - Pruppacher, H. R. and Klett, J. D.: Microphysics of Clouds and Precipitation, Atmospheric and Oceanographic Sciences Library, 18, https://doi.org/10.1007/978-0-306-48100-0, 1997.
 - Reid, J. S., Koppmann, R., Eck, T. F., and Eleuterio, D. P.: A review of biomass burning emissions part II: intensive physical properties of biomass burning particles, Atmospheric Chemistry and Physics, 5, 799–825, https://doi.org/10.5194/acp-5-799-2005, 2005.
- Ren, C. and Mackenzie, A. R.: Cirrus parametrization and the role of ice nuclei, Quarterly Journal of the Royal Meteorological Society, 131, 1585–1605, https://doi.org/10.1256/qj.04.126, 2005.
 - Rolf, C., Krämer, M., Schiller, C., Hildebrandt, M., and Riese, M.: Lidar observation and model simulation of a volcanic-ash-induced cirrus cloud during the Eyjafjallajökull eruption, Atmospheric Chemistry and Physics, 12, 10 281–10 294, https://doi.org/10.5194/acp-12-10281-2012, 2012.

- 850 Sassen, K. and Benson, S.: Ice nucleation in cirrus clouds: A model study of the homogeneous and heterogeneous modes, Geophysical Research Letters, 27, 521–524, https://doi.org/https://doi.org/10.1029/1999GL010883, 2000.
 - Scott, S. G., Bui, T. P., Chan, K. R., and Bowen, S. W.: The Meteorological Measurement System on the NASA ER-2 Aircraft, Journal of Atmospheric and Oceanic Technology, 7, 525 540, https://doi.org/https://doi.org/10.1175/1520-0426(1990)007<0525:TMMSOT>2.0.CO;2, 1990.
- Seifert, A. and Siewert, C.: An ML-Based P3-Like Multimodal Two-Moment Ice Microphysics in the ICON Model, Journal of Advances in Modeling Earth Systems, 16, e2023MS004206, https://doi.org/https://doi.org/10.1029/2023MS004206, e2023MS004206 2023MS004206, 2024.

875

- Skrotzki, J., Connolly, P., Schnaiter, M., Saathoff, H., Möhler, O., Wagner, R., Niemand, M., Ebert, V., and Leisner, T.: The accommodation coefficient of water molecules on ice cirrus cloud studies at the AIDA simulation chamber, Atmospheric Chemistry and Physics, 13, 4451–4466, https://doi.org/10.5194/acp-13-4451-2013, 2013.
- Smith, R. B.: The Influence of Mountains on the Atmosphere, vol. 21 of *Advances in Geophysics*, pp. 87–230, Elsevier, https://doi.org/https://doi.org/10.1016/S0065-2687(08)60262-9, 1979.
- Spichtinger, P. and Cziczo, D. J.: Impact of heterogeneous ice nuclei on homogeneous freezing events in cirrus clouds, Journal of Geophysical Research: Atmospheres, 115, https://doi.org/10.1029/2009JD012168, 2010.
- Spichtinger, P. and Gierens, K.: Modelling of cirrus clouds Part 2: Competition of different nucleation mechanisms, Atmospheric Chemistry and Physics, 9, 2319–2334, https://doi.org/10.5194/acpd-8-9061-2008, 2009.
 - Spichtinger, P. and Krämer, M.: Tropical tropopause ice clouds: a dynamic approach to the mystery of low crystal numbers, Atmospheric Chemistry and Physics, 13, 9801–9818, https://doi.org/10.5194/acp-13-9801-2013, 2013.
- Stevens, B., Moeng, C.-H., and Sullivan, P. P.: Large-Eddy Simulations of Radiatively Driven Convection: Sensitivities to the Representation of Small Scales, Journal of the Atmospheric Sciences, 56, 3963 – 3984, https://doi.org/https://doi.org/10.1175/1520-0469(1999)056<3963:LESORD>2.0.CO;2, 1999.
 - Stevens, B., Moeng, C.-H., Ackerman, A. S., Bretherton, C. S., Chlond, A., de Roode, S., Edwards, J., Golaz, J.-C., Jiang, H., Khairoutdinov, M., Kirkpatrick, M. P., Lewellen, D. C., Lock, A., Müller, F., Stevens, D. E., Whelan, E., and Zhu, P.: Evaluation of Large-Eddy Simulations via Observations of Nocturnal Marine Stratocumulus, Monthly Weather Review, 133, 1443 1462, https://doi.org/10.1175/MWR2930.1, 2005.
 - Sullivan, R. C., Petters, M. D., DeMott, P. J., Kreidenweis, S. M., Wex, H., Niedermeier, D., Hartmann, S., Clauss, T., Stratmann, F., Reitz, P., Schneider, J., and Sierau, B.: Irreversible loss of ice nucleation active sites in mineral dust particles caused by sulphuric acid condensation, Atmospheric Chemistry and Physics, 10, 11 471–11 487, https://doi.org/10.5194/acp-10-11471-2010, 2010.
 - Sölch, I. and Kärcher, B.: A large-eddy model for cirrus clouds with explicit aerosol and ice microphysics and Lagrangian ice particle tracking, Quarterly Journal of the Royal Meteorological Society, 136, 2074–2093, https://doi.org/https://doi.org/10.1002/qj.689, 2010.
 - Thomson, D. S., Schein, M. E., and Murphy, D. M.: Particle Analysis by Laser Mass Spectrometry WB-57F Instrument Overview, Aerosol Science and Technology, 33, 153–169, https://doi.org/10.1080/027868200410903, 2000.
- Tonttila, J., Maalick, Z., Raatikainen, T., Kokkola, H., Kühn, T., and Romakkaniemi, S.: UCLALES–SALSA v1.0: a large-eddy model with interactive sectional microphysics for aerosol, clouds and precipitation, Geoscientific Model Development, 10, 169–188, https://doi.org/10.5194/gmd-10-169-2017, 2017.

- Tully, C., Neubauer, D., Omanovic, N., and Lohmann, U.: Cirrus cloud thinning using a more physically based ice microphysics scheme in the ECHAM-HAM general circulation model, Atmospheric Chemistry and Physics, 22, 11 455–11 484, https://doi.org/10.5194/acp-22-11455-2022, 2022.
- Twohy: Measurements of Saharan Dust in Convective Clouds over the Tropical Eastern Atlantic Ocean, Journal of the Atmospheric Sciences, 72, 75–81, https://doi.org/https://doi.org/10.1175/JAS-D-14-0133.1, 2014.
 - Ullrich, R., Hoose, C., Möhler, O., Niemand, M., Wagner, R., Höhler, K., Hiranuma, N., Saathoff, H., and Leisner, T.: A New Ice Nucleation Active Site Parameterization for Desert Dust and Soot, Journal of the Atmospheric Sciences, 74, 699 717, https://doi.org/10.1175/JAS-D-16-0074.1, 2017.
- Voigt, C., Schumann, U., Minikin, A., Abdelmonem, A., Afchine, A., Borrmann, S., Boettcher, M., Buchholz, B., Bugliaro, L., Costa, A.,
 Curtius, J., Dollner, M., Dörnbrack, A., Dreiling, V., Ebert, V., Ehrlich, A., Fix, A., Forster, L., Frank, F., Fütterer, D., Giez, A., Graf, K., Grooß, J.-U., Groß, S., Heimerl, K., Heinold, B., Hüneke, T., Järvinen, E., Jurkat, T., Kaufmann, S., Kenntner, M., Klingebiel, M., Klimach, T., Kohl, R., Krämer, M., Krisna, T. C., Luebke, A., Mayer, B., Mertes, S., Molleker, S., Petzold, A., Pfeilsticker, K., Port, M., Rapp, M., Reutter, P., Rolf, C., Rose, D., Sauer, D., Schäfler, A., Schlage, R., Schnaiter, M., Schneider, J., Spelten, N., Spichtinger, P., Stock, P., Walser, A., Weigel, R., Weinzierl, B., Wendisch, M., Werner, F., Wernli, H., Wirth, M., Zahn, A., Ziereis, H., and Zöger, M.:
 ML-CIRRUS: The Airborne Experiment on Natural Cirrus and Contrail Cirrus with the High-Altitude Long-Range Research Aircraft HALO, Bulletin of the American Meteorological Society, 98, 271 288, https://doi.org/https://doi.org/10.1175/BAMS-D-15-00213.1, 2017.
- Wendisch, M., Pöschl, U., Andreae, M. O., Machado, L. A. T., Albrecht, R., Schlager, H., Rosenfeld, D., Martin, S. T., Abdelmonem, A., Afchine, A., Araùjo, A. C., Artaxo, P., Aufmhoff, H., Barbosa, H. M. J., Borrmann, S., Braga, R., Buchholz, B., Cecchini, M. A., Costa,
 A., Curtius, J., Dollner, M., Dorf, M., Dreiling, V., Ebert, V., Ehrlich, A., Ewald, F., Fisch, G., Fix, A., Frank, F., Fütterer, D., Heckl, C., Heidelberg, F., Hüneke, T., Jäkel, E., Järvinen, E., Jurkat, T., Kanter, S., Kästner, U., Kenntner, M., Kesselmeier, J., Klimach, T., Knecht, M., Kohl, R., Kölling, T., Krämer, M., Krüger, M., Krisna, T. C., Lavric, J. V., Longo, K., Mahnke, C., Manzi, A. O., Mayer, B., Mertes, S., Minikin, A., Molleker, S., Münch, S., Nillius, B., Pfeilsticker, K., Pöhlker, C., Roiger, A., Rose, D., Rosenow, D., Sauer, D., Schnaiter, M., Schneider, J., Schulz, C., de Souza, R. A. F., Spanu, A., Stock, P., Vila, D., Voigt, C., Walser, A., Walter, D., Weigel, R.,
 Weinzierl, B., Werner, F., Yamasoe, M. A., Ziereis, H., Zinner, T., and Zöger, M.: ACRIDICON–CHUVA Campaign: Studying Tropical Deep Convective Clouds and Precipitation over Amazonia Using the New German Research Aircraft HALO, Bulletin of the American Meteorological Society, 97, 1885 1908, https://doi.org/10.1175/BAMS-D-14-00255.1, 2016.
- Zängl, G., Reinert, D., Rípodas, P., and Baldauf, M.: The ICON (ICOsahedral Non-hydrostatic) modelling framework of DWD and MPI-M: Description of the non-hydrostatic dynamical core, Quarterly Journal of the Royal Meteorological Society, 141, 563–579, https://doi.org/https://doi.org/10.1002/qj.2378, 2015.